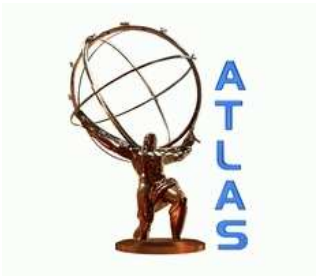

ATLAS NOTE

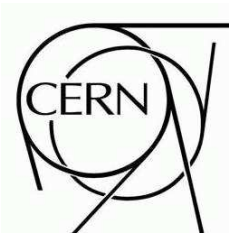

April 28, 2009

Search for the Neutral MSSM Higgs Bosons in the Decay Channel $A/H/h \to \mu^+\mu^-$

The ATLAS Collaboration[1)]

This note is part of CERN-OPEN-2008-020. This version of the note should not be cited: all citations should be to CERN-OPEN-2008-020.

ATL-PHYS-PUB-2009-060
11 May 2009

Abstract

[1)]This note prepared by: H. Bilokon, V. Chiarella, D. Fassouliotis, S. Gentile, S. Horvat, M. Kobel, C. Kourkoumelis, H. Kroha, E.K. Kuznetsova, W.F. Mader, B.R. Mellado Garcia, M. Milosavljevic, G. Nicoletti, K. Nikolopoulos, A. Ruiz-Martinez, J.A. Valls Ferrer, M. Warsinsky.

Motivated by the high muon momentum resolution and identification efficiency achievable with the ATLAS detector, the observability of $A/H/h \to \mu^+\mu^-$ channel is explored. The high experimental resolution in this decay mode compensates to some extent for the suppression of the branching ratio, with respect to the $A/H/h \to \tau^+\tau^-$ decays. The analyses are performed in the Higgs mass range from 100 to 500 GeV. Two main analysis strategies are applied - the search for the dimuon final states resulting from the direct $A/H/h$ production is combined with the search for the associated $b\bar{b}A/H/h$ production mode.

The studies are optimized for the early stage of data taking up to an integrated luminosity of 30 fb^{-1}. All results are obtained combining the fast and the full simulation of the ATLAS detector with the nominal detector layout and the trigger efficiencies included. In addition, dedicated data samples are produced to study the impact of the pile-up and cavern background on the analysis performance. The estimation of the background contribution from the experimental data and the contribution of theoretical and experimental uncertainties are also addressed. The discovery potential is shown in the m_A-tanβ plane in context of the m_h^{max} MSSM benchmark scenario.

1 Introduction

In the framework of the Standard Model, the observability of the Higgs boson in the decay channel $H \to \mu^+\mu^-$ is very unlikely, since the branching ratio for the Higgs decay into muons is very small and the backgrounds from several Standard Model processes are large. As opposed to the Standard Model predictions, the decay of neutral MSSM Higgs bosons A, H and h into two muons is strongly enhanced in the MSSM for large values of $\tan\beta$ and can be used either as a discovery channel or for the exclusion of a large region of the m_A-$\tan\beta$ parameter space (see Ref [1]).

Compared to the dimuon channel, the $A/H/h \to \tau^+\tau^-$ decays have a substantially larger branching ratio which scales as $(m_\tau/m_\mu)^2$ and thus provide a promising discovery signature, as discussed in Ref [2]. Nevertheless, the τ identification represents an experimental challenge. The $\mu^+\mu^-$ final state, on the other hand, has the advantage of a very clear signature in the detector. Furthermore, a full reconstruction of the Higgs boson final state is possible, which allows for a direct mass measurement. The dimuon channel provides for the most accurate Higgs boson mass measurement.

In this note, the potential for the discovery of the neutral MSSM Higgs bosons is evaluated in the dimuon decay channel. The study concentrates on the region of ($m_A - \tan\beta$) plane with $m_A >$110 GeV and intermediate $\tan\beta$ values between 10 and 60, which is still uncovered by the current exprimental limits [3, 4]. A detailed study of the ATLAS discovery potential for this channel has been recently performed in the low mass region below 130 GeV [5]. The study includes also higher Higgs boson masses up to 400 GeV.

In Section 2, the relevant production and decay rates of the MSSM Higgs boson are briefly discussed in the context of the m_h^{max} LHC scenario [6], as well as the production mechanisms of the major background processes. In Section 3, the Monte Carlo simulation and data samples used for the analysis are described. Section 4 provides a short description of the detector performance obtained from the simulation, related to the reconstructed particles which will be present in the final state. The event selection criteria, the resulting efficiency of the signal selection and the corresponding background rejection shall be described in Section 5. Discussion of the systematic uncertainties is presented in Section 6. Section 7 describes the methods for the estimation of different background contributions from the the real data. The obtained results are finally represented by the discovery contours in the (m_A-$\tan\beta$) plane (see Section 9). The note concludes with Section 10.

2 Signal and background processes

In this Section, the properties of the signal shall be briefly described, as well as the background processes relevant for the MSSM Higgs boson searches in the dimuon final state at the LHC.

2.1 Signal production and decays

The characteristic production and decay properties of all MSSM Higgs bosons are determined at tree-level by the values of the two free parameters $\tan\beta$ and the mass m_A of the A boson. These properties have been calculated at NNLO with the Feynhiggs 2.6.2 package [7] in the m_h^{max} scenario, as summarized in Ref [1].

The direct $gg \to A/H/h$ production via the gluon-gluon fusion is an analogue to the Standard Model Higgs boson production. This process is important in the region of low $\tan\beta$ values (below 10), where the Higgs bosons couple most strongly to up-type quarks. For larger values of $\tan\beta$, the rate of the $b\bar{b}A/H/h$ Higgs production in association with b-quarks becomes dominant, due to the enhanced couplings to the b-quarks.

There are two approaches to calculate the signal rates for the associated $b\bar{b}A/H/h$ production mode. In the first approach, the production cross-section for the $gg \to b\bar{b}H$ process has been calculated at NLO in Ref [8, 9]. This calculation is most reliable in the case where both outgoing b-quarks have a high transverse momentum (above $\sim$15 GeV). The inclusive cross-section without any cut on the transverse momenta of the b-quarks is less accurate, due to additional collinear logarithms which appear in the calculation due to the presence of low-momentum b-quarks. An alternative approach is the calculation of the inclusive cross-section for the $b\bar{b} \to H$ process, for which the collinear logarithms can be absorbed in a parton density function for the b-quarks and resummed to all orders of perturbation theory [10, 11]. This later calculation has been implemented in a parametrized way into the Feynhiggs package, which was finally used for the evaluation of the signal cross-sections, as mentioned previously.

The different higher-order calculations mentioned above have been extensively compared in Ref [12]. The two approaches agree within uncertainties. For the $gg \to b\bar{b}H$ calculation, the uncertainty related to the variation of the renormalization and the factorization scale amounts to 20-30%. For the $b\bar{b} \to H$ calculation, which is used for the analysis, the scale uncertainty is much smaller, less than 10%. However, it should be noted that the uncertainty on the b parton density function has not been included here. In order to estimate this pdf-uncertainty, a calculation of the $b\bar{b} \to H$ cross-section is performed with two different parton density functions, MRST2002 and MRST2004. The observed difference of $\sim$14% is taken as the estimate of the pdf-uncertainty. Adding the 10% scale uncertainty to this in quadrature, the total theory uncertainty for the signal is estimated to be $\sim$17% for H boson masses up to 500 GeV.

The production cross-section of H and A bosons increases approximately quadratically with increasing $\tan\beta$, while the h boson production is $\tan\beta$-dependent only for $m_A <$130 GeV. Also the branching ratio of H and A boson decays into $\mu^+\mu^-$ pairs become enhanced with increasing values of $\tan\beta$. The h boson decay is rather insensitive to the two mentioned parameters. The increase of the cross-sections and branching ratios with $\tan\beta$ make the $A/H/h \to \mu^+\mu^-$ decay channel a promising Higgs signature in MSSM.

Additionally, the signal is enhanced due to the mass degeneracy of the neutral Higgs bosons. For A boson masses $m_A <$130 GeV, the h and A bosons are degenerate in mass, while the heavy H boson mass is rather constant ($\sim$130 GeV). In case of $m_A \approx$130 GeV, all three bosons have very similar masses. For $m_A >$130 GeV, the h boson mass reaches its maximum value of $\sim$130 GeV, independent of the A boson mass, while the A and H bosons become degenerate in mass. Thus the signal can be observed as the sum of all two or three degenerate mass states.

2.2 Background processes

The processes with two muons in the final state, which give a major background contribution in the searches for the $A/H/h$ signal are depicted in Figure 1.

The dominant background process with a very large production rate of $\sim$1 nb is the Drell-Yan Z boson production, with subsequent Z decay into two muons. The invariant dimuon mass peaks at the Z resonance, such that the search for the $A/H/h$ becomes unfeasible for the Higgs masses below 100 GeV. Even for the higher Higgs boson masses, the tail of the Z resonance still provides an overwhelming background. The Drell-Yan background can be suppressed by requiring the presence of one or more additional b-jets, originating from the associated $b\bar{b}A$ production. The major backgrounds remaining after this requirement are the Z boson production in association with the light jets or b-jets and the $t\bar{t} \to (W^+b)(W^-\bar{b}) \to (\mu^+\nu b)(\mu^-\nu\bar{b})$ background. The $t\bar{t}$ background can be distinguished from the signal by a higher jet activity and a large missing energy caused by the neutrinos from W decays. Additional background from WW and ZZ diboson productions is expected to be small, due to the much lower production rates.

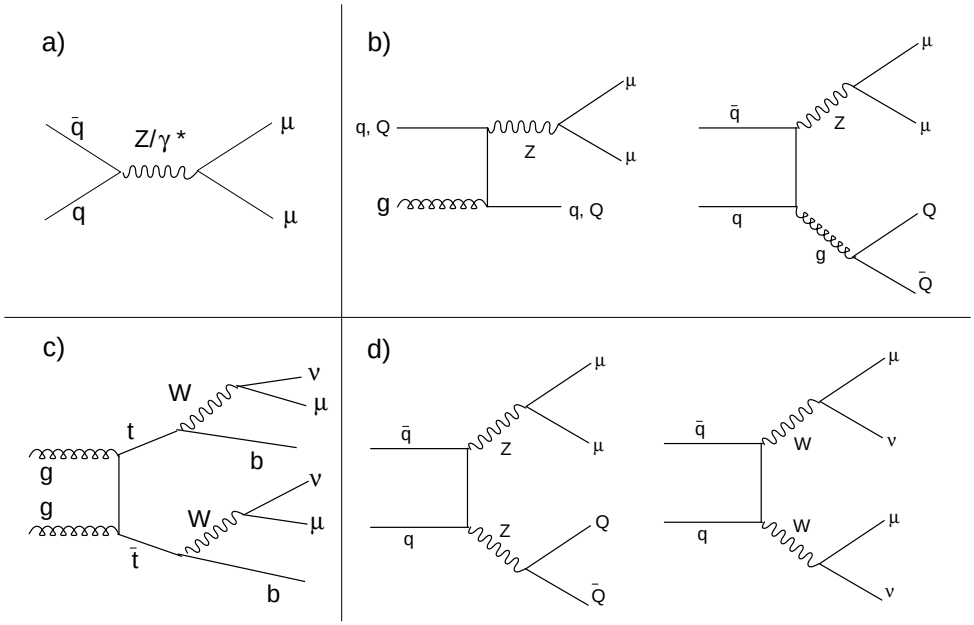

Figure 1: Tree-level Feynman diagrams of the dominant background processes with two isolated muons in the final state: a) Drell-Yan Z boson production, b) Z boson production in association with jets, c) $t\bar{t}$ production and d) ZZ and WW production. q is a general symbol for u and d quarks, while Q stands for the b and c quarks.

3 Data samples

Two different Monte Carlo generators are used for the signal production. PYTHIA 6.4 [13] has been used to generate the direct $gg \to \phi \to \mu\mu$ and associated $gg \to b\bar{b}\phi \to b\bar{b}\mu\mu$ processes (where $\phi = A,\ H,\ h$). The SHERPA [14] event generator (version 1.0.9) combines all three associated production mechanisms, $gg \to b\bar{b}\phi$, $bg \to b\phi$ and $b\bar{b} \to \phi$, in a coherent way without double-counting. This is accomplished by the CKKW algorithm [15] for the matching of the parton showers to the quark emission from the matrix elements. Both generators provide leading-order cross-sections, which have been rescaled to the Feynhiggs NNLO values. The studies at the D0 experiment [16] have shown that the differential SHERPA distributions are in a good agreement with the real data and can simply be normalized to the previously described inclusive higher-order cross-sections. The comparison of the samples produced by the two generators will be described in Section 6.1. A generator filter requiring at least two muons with p_T >5 GeV and $|\eta|$ <2.7 is applied to each event for all signal data samples, after the showering and before writing out the events into permanent storage. The background samples are listed in Table 1, together with the corresponding NLO cross-sections. The details of the cross-section computation can be found in Ref [17]. In addition to already mentioned generators, the MC@NLO 3.1 [18] and AcerMC 3.4 packages [19] have been used for the event generation.

Full simulation of the detector response has been performed for all signal and background event topologies, within the ATHENA software framework which uses the GEANT4 [20] package for the description of the detector response. In addition, due to the large background production rates, it is necessary to increase the number of simulated events by means of the parametrized fast detector simulation (Atlfast [21]). The presented analyses are based on the combination of both simulation types. The samples obtained with the detailed simulation have been used for the tuning of the parametrized description of the detector performance in the fast simulation. The tuning procedure provides a very good agreement

with the full detector simulation. Any remaining differences are treated as systematic uncertainty.

Process	Generator	$\sigma \times BR$ [pb]	Filter efficiency	Number of events	Simulation type
$t\bar{t}$; 2μ-filter	MC@NLO	833	0.072	500 000	full sim.
$t\bar{t}$; 1ℓ-filter	MC@NLO	833	0.556	600 000	full sim.
$(Z \to \mu\mu)$+0-3 light jets	SHERPA	2036	0.490	5 000	full sim.
$(Z \to \mu\mu)$+1-3 b-jets	SHERPA	52.3	0.914	5 000	full sim.
$b\bar{b}(Z \to \mu\mu)$	AcerMC/PYTHIA	45	0.788	280 000	full sim.
$ZZ \to bb\mu\mu$	PYTHIA	0.151	0.724	10 000	full sim.
WW	PYTHIA	116.8	0.35	50 000	full sim.
$t\bar{t}$, no filter	MC@NLO	833.0	1.0	100 000 000	Atlfast
$(Z \to \mu\mu)$+0-3 light jets	SHERPA	1165.9	0.855	30 000 000	Atlfast
$(Z \to \mu\mu)$+0-3 b-jets	SHERPA	52.3	0.914	1 000 000	Atlfast

Table 1: Background data samples with corresponding NLO cross-sections.

All mentioned data samples have been simulated assuming there are no additional pp-interactions per event. However, at luminosities of 10^{33} cm^{-2}s^{-1} one expects to have 2-3 such pile-up interactions superimposed to the hard scattering. In addition, the neutron and photon background of the muon spectrometer (so called cavern background) may increase the muon trigger rate and degrade the muon reconstruction performance [22]. In order to study the impact of the pile-up and cavern background on the analysis performance, dedicated $b\bar{b}A$, $t\bar{t}$ and $Zb\bar{b}$ data samples have been simulated with the realistic pile-up and cavern background contribution. The simulated cavern background is assumed to be five times higher than the prediction of GCALOR [23] and FLUKA [24] simulations, to account for the uncertainty of the calculation.

4 Detector performance

A detailed description of the ATLAS detector and its performance is given in Ref [25]. The details of the detector layout, the software framework used for the Monte Carlo production, as well as the details of the reconstruction of fully simulated events can be found in Ref [26]. In this Section, the performance of the reconstruction algorithms is shortly described, concentrating on the key objects for the analyses: muon identification and momentum measurement, jet reconstruction, b-tagging and the measurement of the missing transverse energy (E_T^{miss}). First, the results obtained in absence of pile-up and cavern background in the detector are shown. These are subsequently compared to the results obtained when both pile-up and cavern background are taken into account.

4.1 Reconstruction performance without pile-up and cavern background

In ATLAS, the muon reconstruction is performed by combining the information of the muon spectrometer and the inner detector. Staco and MuTag [22] reconstruction packages are used for the study. The average muon reconstruction efficiency is (97.15$\pm$0.04)%. This is reduced to (95.44$\pm$0.05)% if a match between the muon spectrometer track and the inner detector track is required. The momentum resolution of low-p_T muons is mostly dominated by the inner detector performance, while the high-p_T muon reconstruction is more sensitive to the muon spectrometer performance. The average muon momentum resolution is better than 3%, which allows for an excellent dimuon mass resolution, as shown in Figure 2

for the A-boson (m_A=200 GeV) produced via the associated $b\bar{b}A$ and the direct $gg \to A$ production mode. As expected, the experimental dimuon mass resolution does not depend on the Higgs production mode. Table 2 summarizes the dimuon mass resolutions obtained for different A boson masses.

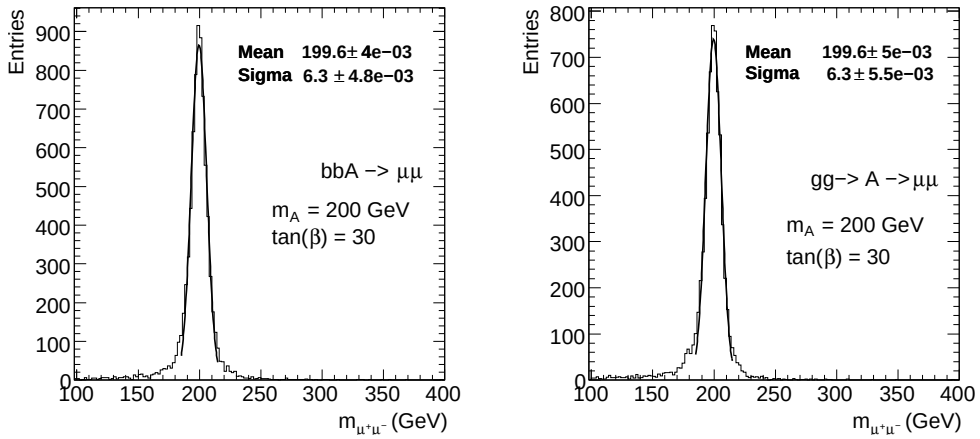

Figure 2: Dimuon mass distribution for the $b\bar{b}A$ and $gg \to A$ signal samples with an A boson mass of 200 GeV and $\tan\beta$=30. The distributions are fitted by the Gauss function.

	A boson mass (GeV)					
(GeV)	110	130	150	200	300	400
Natural width	2.16	2.48	2.80	3.60	5.61	8.46
Reconstructed σ	2.59 ± 0.02	3.83 ± 0.03	4.11 ± 0.04	6.29 ± 0.05	10.2 ± 0.2	15.0 ± 0.3
Reconstructed mass	109.818 $\pm$ 0.006	129.738 $\pm$ 0.005	149.796 $\pm$ 0.006	199.589 $\pm$ 0.005	298.82 $\pm$ 0.04	399.37 $\pm$ 0.04

Table 2: The natural width of the A boson and the expected width of the dimuon resonance based on Monte Carlo simulated data are shown for the $b\bar{b}A$ signal at different mass points and with $\tan\beta$=30.

Characteristic of the $b\bar{b}A$ signal are the b-jets with generally rather low transverse momenta, as shown in Figure 3(a). Since the efficiency of the b-jet reconstruction decreases with the p_T, the number of reconstructed b-jets will in general be smaller for the signal than for the $t\bar{t}$ or $ZZ \to bb\mu\mu$ backgrounds, where the b-jets are more energetic (see Figure 3(b)). A detailed study was performed to identify the optimum b-jet selection criteria. The best jet reconstruction performance is observed for the jet cone algorithms with the cone size of $\Delta R = \sqrt{\Delta\eta^2 + \Delta\phi^2} = 0.4$, compatible with the performance of the k_T algorithm for the same cone size. After a jet is selected as described, the b-tagging algorithm is performed to determine whether the jet originates from the b-quark. The minimum p_T value of 20 GeV is required for each b-jet in order to reduce the contribution of the calorimeter noise and of the mistagged light- or c-jets. The rejection of light- and c-jets is essential for the suppression of the $Z + jet$ background. One could extend the lower p_T-bound down to $\sim$15 GeV without a large change of the rejection rate. However, the impact on the final signal significance will be rather small, while the agreement between the full and the fast simulation is shown to decrease.

Several b-tagging algorithms have been studied in order to define the optimum selection of the low-p_T b-jets coming from the signal. The best rejection is obtained by IP3DSV1 [27], which is based on the

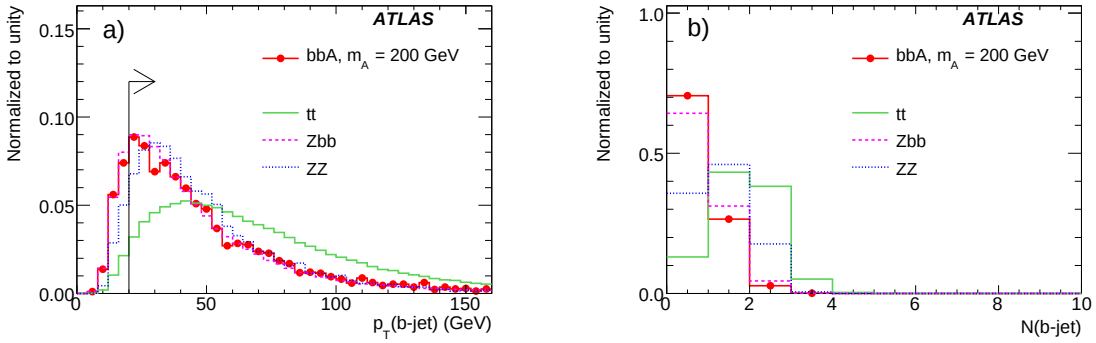

Figure 3: a) Transverse momentum p_T of the b-jets in the $b\bar{b}A$ signal and the dominant background processes and b) the number of reconstructed b-jets per event. The selection criteria for the b-jets are described in the text.

information obtained from the transverse and longitudinal impact parameter significances of the tracks and from the reconstructed secondary vertex. The distribution of the b-tagging weight obtained by this algorithm is shown in Figure 4 for the b-jets and the light jets in the $b\bar{b}A$ signal sample at 200 GeV and in the $t\bar{t}$ background sample. The arrow indicates the optimum cut value of 4. Figure 5 shows the

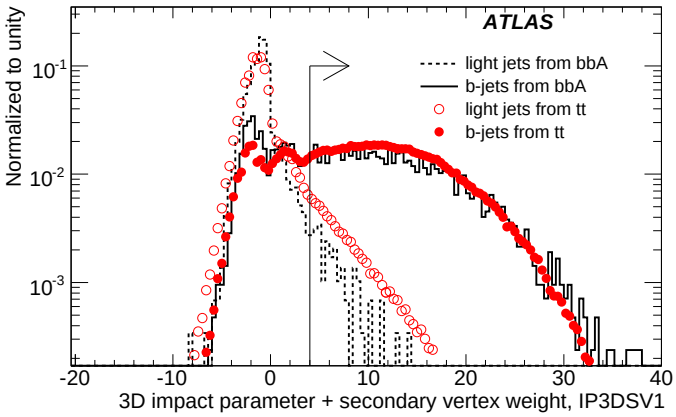

Figure 4: Distribution of the b-tagging weight for the b-jets and the light jets in the $b\bar{b}A$ signal and $t\bar{t}$ background sample, obtained by the IP3DSV1 b-tagging algorithm. The arrow indicates the optimum cut value of 4, which is used for the selection of the b-jets in the analyses.

obtained b-tagging efficiency for the $b\bar{b}A$ signal sample, in dependence on the b-jet E_{T} (Figure 5a)) and η (Figure 5b)). The kinematic cuts of p_T >20 GeV and $|\eta| < 2.5$, as well as the IP3DSV1 weight-cut of 4 have been applied for the b-jet selection. The resulting b-tagging efficiency is (64.1±0.81)% for the $b\bar{b}A$ signal sample, with a light-jet rejection of (80±1) for the $Z+jet$ sample. Systematic detector-related uncertainties are not included here.

The final important reconstruction object is the missing transverse energy (E_T^{miss}), which allows for the suppression of the $t\bar{t}$ background. In the signal processes, there is no neutrino contribution, such that the measured E_T^{miss} value is dominated by the experimental resolution. The reconstruction algorithm for

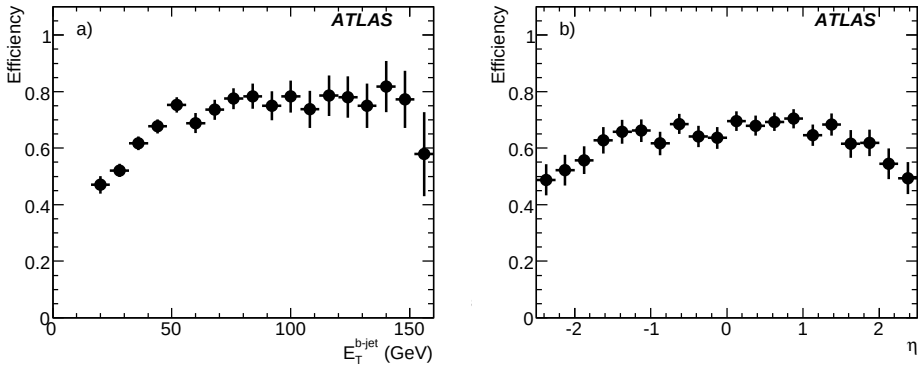

Figure 5: B-tagging efficiency in dependence of b-jet transverse energy E_{T} (a) and pseudorapidity η (b), evaluated for the $b\bar{b}A$ signal sample at m_A =200 GeV and $\tan\beta$ =30. IP3DSV1 b-tagging weight cut of >4 has been applied.

the calculation of the missing transverse energy is described in detail in Ref [28]. The distributions of $E_{T(x,y)}^{miss}$ components in the signal samples have a Gaussian part with a width σ=(7.8±0.1) GeV, while the non-Gaussian tails (above 5σ) are found to contribute less than 1.5% to the overall distribution. E_T^{miss} is sensitive to pile-up effects, as will be described in the next subsection.

4.2 Reconstruction performance under influence of pile-up and cavern background

In the following, the detector performance related to the analysis is evaluated in dependence on the pile-up at luminosities of 10^{33} cm^{-2}s^{-1} and cavern background (five times higher than the expectation). In Figure 6(left), the efficiency and the fake rate of the muon reconstruction is shown for the $b\bar{b}A$ signal sample simulated without and with the pile-up contribution as a function of the pseudorapidity. The corresponding momentum resolution is shown in Figure 6(middle). Similar results are obtained also for the background samples. As can be seen from the plots, muon reconstruction is only marginally

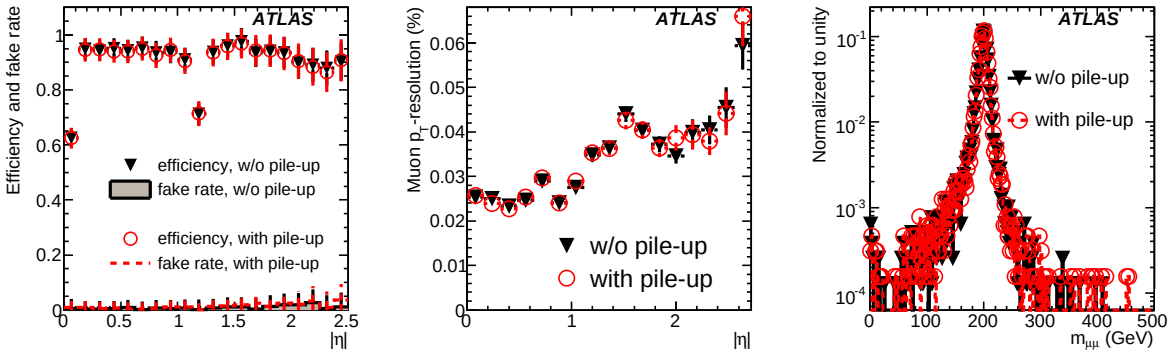

Figure 6: Efficiency and the fake rate (left) and resolution (middle) of the muon reconstruction as a function of the $|\eta|$ (for p_T >20 GeV), with and without the pile-up contribution in the $b\bar{b}A$ signal sample with m_A=200 /GeV. The right plot shows the corresponding dimuon mass distribution.

influenced by pile-up. Consequently, the dimuon invariant mass also remains unaffected, as shown in

Figure 6(right) for m_A=200 GeV.

On the contrary, the reconstruction of the missing transverse energy is substantially affected by pile-up in the calorimeter. The degradation of the E_T^{miss}-resolution mainly affects the selection of events with a small true missing energy (signal and the Z background) as shown in Figure 7(left); $t\bar{t}$ events, characterized by a large missing energy, are rather insensitive to pile-up (see Figure 7(right)). This

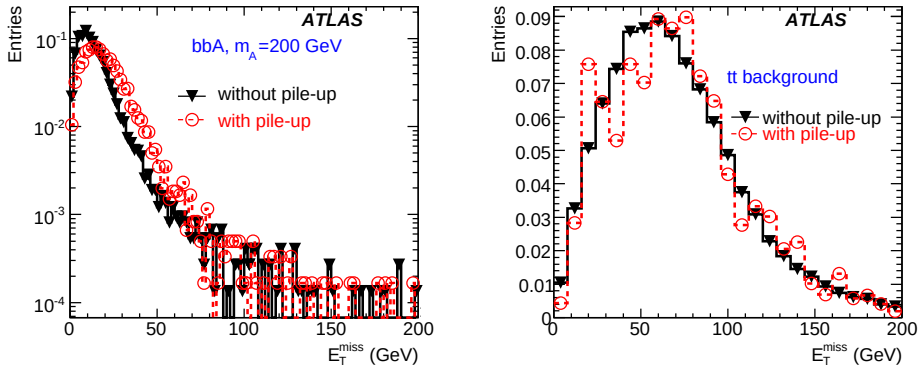

Figure 7: Missing transverse energy distribution for the $b\bar{b}A$ signal at 200 GeV (left) and the $t\bar{t}$ background (right),with and without pile-up.

effect must be taken into account during the optimization of the event selection criteria. For instance, an event selection cut at E_T^{miss} <30 GeV, which is reasonable without pile-up, would reject too many signal events, once the pile-up contribution is included. Therefore, this analysis cut should rather be set to at least 40 GeV in the realistic LHC environment.

The change of the calorimeter response under the influence of pile-up affects also the jet reconstruction. Due to a higher calorimeter activity, one expects an increase in the number of reconstructed jets. This can be observed in Figure 8(left), showing the jet multiplicity in the $Zb\bar{b}$ background events.

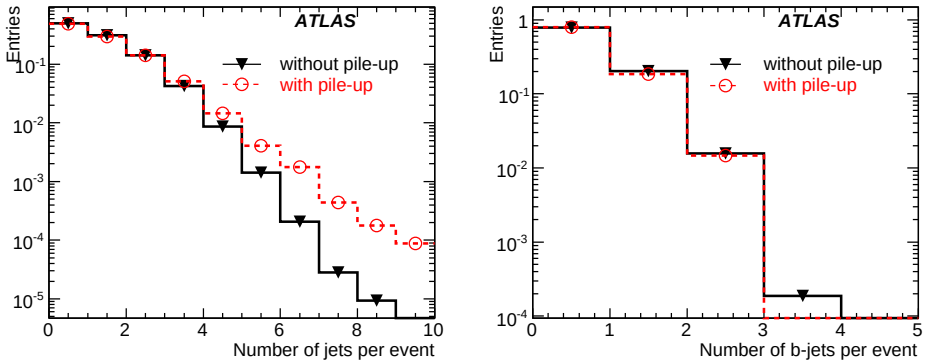

Figure 8: Total number of jets per event (left) and the number of b-jets (right) in the $Zb\bar{b}$ background sample, with and without the pile-up contribution.

No significant impact of the pile-up is observed on the b-tagging (see Figure 8(right)), due to the additional tracking and vertex information.

5 Event selection

The search for the MSSM Higgs bosons can be performed by several different approaches, related to the number of jets one requires to be present in the final state. As mentioned before, due to a large signal production rate in the associated production mode, the presence of the b-jets in the final state can help to suppress the Drell-Yan background. On the contrary, the remaining events with 0 b-jets provide for a high signal rate on top of the smoothly distributed background, even at low integrated luminosity.

The event selection methods are optimized separately for the two cases:

- Signatures with 0 b-jets in the final state.
- Signatures with at least one b-jet in the final state.

The two mentioned final states are uncorrelated and therefore complementary. In the case of 0 b-jets in the final state, the dominant background is the Drell-Yan Z boson production, while in the case of at least one b-jet the $t\bar{t}$ background has the biggest contribution, especially for Higgs masses above 130 GeV, which are further away from the Z resonance.

Before describing the selection criteria, the preselection of the events is discussed, common to the two signatures above. The preselection is defined by the kinematic cuts on muon p_T and $|\eta|$, together with the muon isolation criteria.

5.1 Preselection

The main characteristics of the signal signatures is the presence of two isolated muons of opposite charge in the final state. The p_T-distribution of the muons is shown in Figure 9 for the signal and background processes. The signal is characterized by the relatively high-p_T muons, while the background has muons

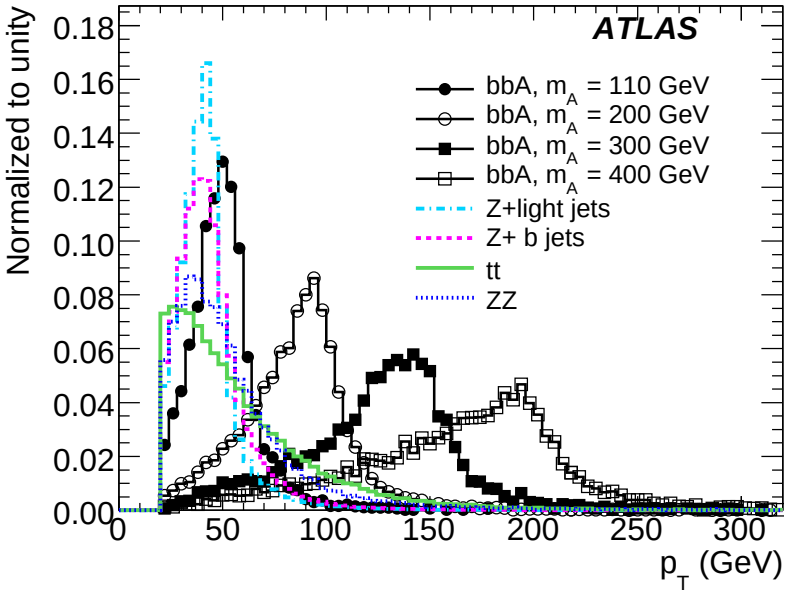

Figure 9: Distribution of the muon transverse momentum p_T for the muons in the signal and background events.

of lower momenta. The muon p_T distribution in the signal is highly correlated to the Higgs boson mass. Therefore, the lower bound on the muon p_T is kept at a relatively low value, in order to allow for a general search in a broad Higgs mass range. At preselection level, both muons are required to have a p_T >20 GeV and to be in the pseudorapidity range $|\eta|$ <2.7.

The selected high-p_T muons are required to be isolated, in order to reject the processes in which the muons originate from the hadronic decays. The applied isolation criteria require the calorimeter energy E_T deposited in a cone of size ΔR = 0.4 around a given muon, divided by the muon p_T to be lower than 0.2. The distribution of this isolation variable is shown in Figure 10(left) for different signal and background processes.

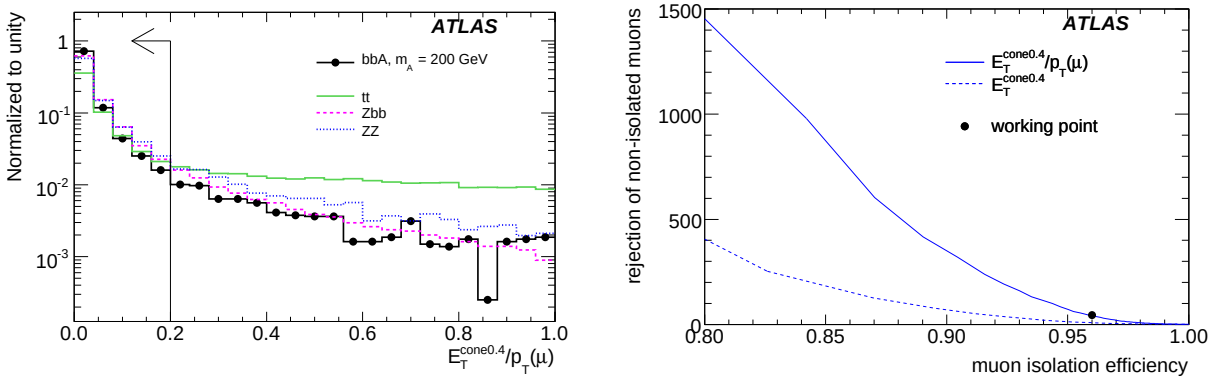

Figure 10: (left) Muon isolation variable $E_T^{cone0.4}/p_T(\mu)$, shown for different signal and background processes. Here, the $E_T^{cone0.4}$ is the energy measured in the calorimeters in cone $\Delta R = 0.4$ around a given muon. (right) Rejection of the non-isolated muons originating from the b-quarks in $t\bar{t}$ events as a function of the selection efficiency for isolated muons, shown for the two isolation variables described in the text. The filled circle indicates the working point with the isolation cut at $E_T^{cone0.4}/p_T(\mu)$ <0.2 .

The isolation criteria significantly decrease the $t\bar{t}$ background, where one of the muons comes from the b-decays. The power of rejection of the non-isolated muons originating from the b-quarks in the $t\bar{t}$ background is shown in Figure 10(right) for the standard calorimeter isolation ($E_T^{cone0.4}$), and for the isolation normalized by the muon p_T.

Due to the high muon momenta, the signal can be efficiently triggered by the single high-p_T muon trigger. The efficiency of the trigger selection for the dimuon signal events is shown to be around 95% for all studied mass points. The detailed study of the trigger selection efficiency for events which pass all offline event selection criteria will be presented in Section 5.3. In the following, the results of the event selection without the trigger requirement are presented at first.

5.2 Signatures with 0 b-jets and with at least one b-jet in the final state

The large Z boson background contribution can be reduced by requiring that the jets which are present in the final state are tagged as b-jets. Therefore, assuming a fully performing b-tagging algorithm, the following set of selection criteria can be applied:

- Events are required to pass the preselection criteria and to have a missing transverse energy E_T^{miss} <40 GeV. This cut is particularly effective in rejecting the $t\bar{t}$ and WW background, which

are characterized by a high missing energy due to the presence of neutrinos in the final state (see Figure 11(left)).

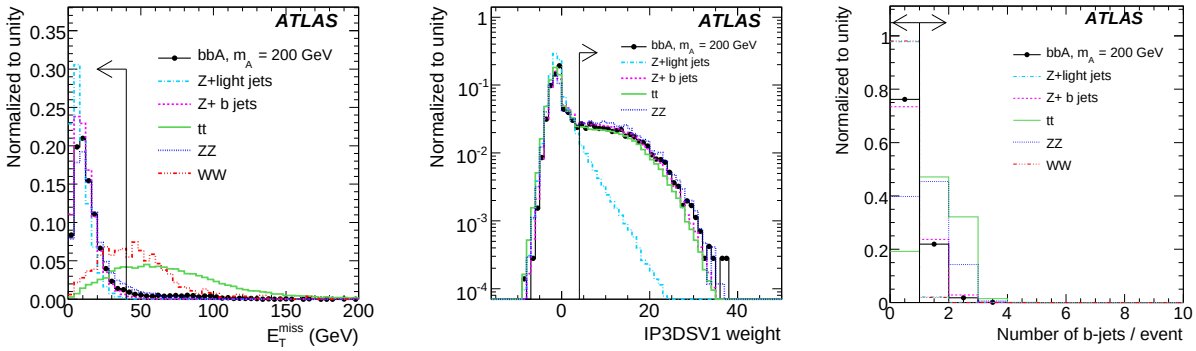

Figure 11: (left) Missing transverse energy, (middle) distribution of the b-tagging IP3DSV1 weight after requiring p_T >20 GeV and $|\eta|$ <2.5 and (right) the multiplicity of reconstructed b-jets per event, after applying the p_T- and η-cuts and requiring the b-tagging IP3DSV1 weight greater than 4. Distributions for the *bbA* signal (m_A=200 GeV) and for the major background processes are shown. Arrows indicate the cuts applied in the analysis.

- Subsequently, the number of b-jets is counted in each event, requiring p_T >20 GeV, $|\eta|$ <2.5 and the b-tagging IP3DSV1 weight greater than 4. The distribution of the b-tagging weights before and the b-jet multiplicity after applying the weight-cut are shown in Figure 11. As shown in the middle plot, the b-tagging weight is effective in reducing the background from $Z+light\ jets$, at the expense of a significant loss of the signal. This cut is scarcely effective against the $t\bar{t}$ background, which, however, can be reduced by the additional cuts discussed below. Therefore, the analysis is divided into a channel with 0 b-jets (in which the Z background is dominant) and the channel with at least one b-jet (in which the $t\bar{t}$ background plays an important role and can be further suppressed).

- Further $t\bar{t}$ rejection criteria have been studied for the channel with at least one b-jet.

  – Two muons originating from the decay of the same particle (Higgs boson) tend to be emitted back-to-back, especially if this particle has a low transverse momentum. As opposed to that, the muons originating from the two different particles (as in the $t\bar{t}$ events) are not correlated and can be separated by any angle. Therefore, the cut is applied on the angle $\Delta\phi_{\mu\mu}$ between the two muons by requiring $|\sin\Delta\phi_{\mu\mu}|$ <0.75. The $|\sin\Delta\phi_{\mu\mu}|$ distributions for the signal and background processes are shown in Figure 12(a).

  – In addition, several discriminating variables related to the hadronic activity in the events have been studied: the p_T distribution of the b-jets, the number of jets per event, or a sum of the transverse momenta of all jets in the event ($\sum p_T^{jet}$). The distributions of two of these variables are shown in Figure 12b) and c). The latter is shown to provide the highest rejection against the $t\bar{t}$ background, while at the same time remaining relatively robust under the the influence of pile-up. A cut at $\sum p_T^{jet}$ <90 GeV is required.

- The final number of events which is used for the calculation of the signal significances is evaluated in a mass window Δm=$m_A\pm 2\sigma_{\mu\mu}$ around the A boson mass, where $\sigma_{\mu\mu}$ is the expected

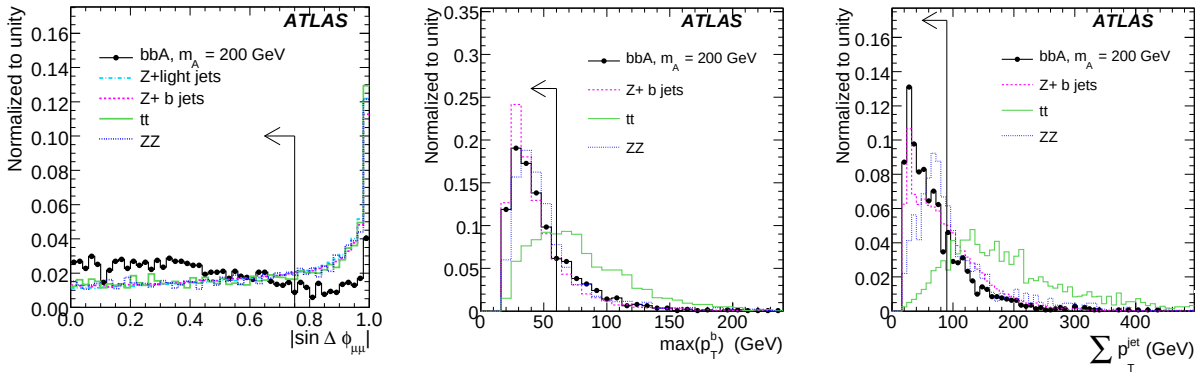

Figure 12: Discriminating variables against the $t\bar{t}$ background: a) $|\sin\Delta\phi|$ shown for the $b\bar{b}A$ signal (m_A=200 GeV) and for the major background processes, b) the maximum p_T of the b-jet, and c) $\sum p_T^{jets}$-distribution for the signal and background processes. Arrows indicate the cuts applied in the analysis.

m_A-dependent width of the dimuon resonance (see Table 2).

The signal and background event rates after each of the cuts described above are shown in Tables 3 and 4.

Cut	bbA **(fb)** 130 GeV	bbA **(fb)** 150 GeV	bbA **(fb)** 200 GeV	bbA **(fb)** 300 GeV	bbA **(fb)** 400 GeV	$gg \to A$ **(fb)** 200 GeV
All events	$13.4{\cdot}10^{1}$	$8.7{\cdot}10^{1}$	$31.5{\cdot}10^{0}$	$6.9{\cdot}10^{0}$	$19.3{\cdot}10^{-1}$	$32.3{\cdot}10^{-1}$
muon preselection	$8.8(2){\cdot}10^{1}$	$5.9(1){\cdot}10^{1}$	$22.3(3){\cdot}10^{0}$	$5.0(1){\cdot}10^{0}$	$14.4(3){\cdot}10^{-1}$	$28.6(3){\cdot}10^{-1}$
E_T^{miss} <40 GeV	$8.3(2){\cdot}10^{1}$	$5.4(1){\cdot}10^{1}$	$20.3(2){\cdot}10^{0}$	$4.4(1){\cdot}10^{0}$	$11.7(2){\cdot}10^{-1}$	$25.9(3){\cdot}10^{-1}$
nr. of b-jets=0	$6.6(1){\cdot}10^{1}$	$4.3(1){\cdot}10^{1}$	$15.5(2){\cdot}10^{0}$	$31.6(8){\cdot}10^{-1}$	$8.2(2){\cdot}10^{-1}$	$25.1(3){\cdot}10^{-1}$
Δm	$\mathbf{5.6(1){\cdot}10^{1}}$	$\mathbf{34.1(8){\cdot}10^{0}}$	$\mathbf{128.0(1){\cdot}10^{-1}}$	$\mathbf{26.4(8){\cdot}10^{-1}}$	$\mathbf{6.9(2){\cdot}10^{-1}}$	$\mathbf{204.2(1){\cdot}10^{-2}}$
nr. of b-jets≥1	$16.2(7){\cdot}10^{0}$	$11.2(5){\cdot}10^{0}$	$4.8(1){\cdot}10^{0}$	$12.1(5){\cdot}10^{-1}$	$3.5(1){\cdot}10^{-1}$	$8.2(5){\cdot}10^{-2}$
$\lvert\sin\Delta\phi_{\mu\mu}\rvert$ <0.75	$11.7(6){\cdot}10^{0}$	$8.3(4){\cdot}10^{0}$	$4.0(1){\cdot}10^{0}$	$10.7(5){\cdot}10^{-1}$	$3.2(1){\cdot}10^{-1}$	$4.8(4){\cdot}10^{-2}$
$\sum p_T^{jets} < 90$ GeV	$9.3(5){\cdot}10^{0}$	$6.5(3){\cdot}10^{0}$	$2.9(1){\cdot}10^{0}$	$7.1(4){\cdot}10^{-1}$	$1.7(1){\cdot}10^{-1}$	$2.0(3){\cdot}10^{-2}$
Δm	$\mathbf{8.3(5){\cdot}10^{0}}$	$\mathbf{5.3(3){\cdot}10^{0}}$	$\mathbf{23.9(8){\cdot}10^{-1}}$	$\mathbf{5.9(4){\cdot}10^{-1}}$	$\mathbf{14.8(8){\cdot}10^{-2}}$	$\mathbf{1.7(3){\cdot}10^{-2}}$

Table 3: $\sigma \times BR$ for the signal processes at $\tan\beta$=30 after each selection cut. Numbers in brackets represent the statistical error on the last digit.

A signal selection efficiency of 7-10% is reached for the channel with at least one b-jet in the final state. The dominant background processes are almost equally the $Z+jet$ and the $t\bar{t}$ events. The signal events are mainly lost due to the limited b-jet reconstruction efficiency, as discussed previously. This is in agreement with a much larger signal selection efficiency of 40-50% in the case of the channel with 0 b-jets. Here, the Z background is observed to have a dominant contribution. The invariant dimuon mass distributions obtained for the two channels are shown in Figure 13.

In the initial phase of the detector running, the b-tagging algorithms still may not have the optimum performance. Therefore, the discovery potential has also been evaluated for the case where no b-tagging requirement is imposed on the reconstructed jets. Due to the large Z background, the signatures with no b-tagging requirement will provide a similar discovery potential as the analysis with 0 b-jets in the final state.

Cut	$Z+light\ jet$ **(fb)**	$Z+b\ jet$ **(fb)**	$t\bar{t}$ **(fb)**	$ZZ \to bb\mu\mu$ **(fb)**	WW **(fb)**	Total
All events	$2036.0 \cdot 10^{3}$	$52.3 \cdot 10^{3}$	$833.0 \cdot 10^{3}$	151.0	$116.8 \cdot 10^{3}$	
muon preselection	$727.7(2) \cdot 10^{3}$	$333.8(4) \cdot 10^{2}$	$57.6(1) \cdot 10^{2}$	$61.3(8) \cdot 10^{0}$	$6.7(2) \cdot 10^{2}$	
E_T^{miss} <40 GeV	$726.2(2) \cdot 10^{3}$	$330.1(4) \cdot 10^{2}$	$132.7(6) \cdot 10^{1}$	$56.1(8) \cdot 10^{0}$	$3.0(2) \cdot 10^{2}$	
nr. of b-jets=0	$710.7(2) \cdot 10^{3}$	$242.3 \cdot 10^{2}$	$25.6(3) \cdot 10^{1}$	$22.3(5) \cdot 10^{0}$	$2.9(2) \cdot 10^{2}$	
Δm (130 GeV)	$\mathbf{35.4(1) \cdot 10^{2}}$	$\mathbf{8.8(2) \cdot 10^{1}}$	$\mathbf{20.2(8) \cdot 10^{0}}$	$\mathbf{1.5(4) \cdot 10^{-1}}$	$\mathbf{1.8(4) \cdot 10^{1}}$	$\mathbf{3.7(1) \cdot 10^{3}}$
Δm (150 GeV)	$\mathbf{152.5(8) \cdot 10^{1}}$	$\mathbf{3.4(1) \cdot 10^{1}}$	$\mathbf{16.0(7) \cdot 10^{0}}$	$\mathbf{0.7(3) \cdot 10^{-1}}$	$\mathbf{2.6(5) \cdot 10^{1}}$	$\mathbf{15.9(1) \cdot 10^{2}}$
Δm (200 GeV)	$\mathbf{58.9(5) \cdot 10^{1}}$	$\mathbf{8.4(7) \cdot 10^{0}}$	$\mathbf{11.6(6) \cdot 10^{0}}$	$\mathbf{0.6(1) \cdot 10^{-1}}$	$\mathbf{1.6(3) \cdot 10^{1}}$	$\mathbf{62.5(6) \cdot 10^{1}}$
Δm (300 GeV)	$\mathbf{18.1(3) \cdot 10^{1}}$	$\mathbf{1.8(3) \cdot 10^{0}}$	$\mathbf{5.1(4) \cdot 10^{0}}$	$\mathbf{0.1(1) \cdot 10^{-1}}$	$\mathbf{0.2(2) \cdot 10^{1}}$	$\mathbf{19.0(4) \cdot 10^{1}}$
Δm (400 GeV)	$\mathbf{7.8(2) \cdot 10^{1}}$	$\mathbf{0.8(2) \cdot 10^{0}}$	$\mathbf{2.0(2) \cdot 10^{0}}$	$\mathbf{0.1(1) \cdot 10^{-1}}$	$\mathbf{0.2(2) \cdot 10^{1}}$	$\mathbf{8.4(3) \cdot 10^{1}}$
nr. of b-jets≥1	$154.9(3) \cdot 10^{2}$	$87.7(2) \cdot 10^{2}$	$107.1(6) \cdot 10^{1}$	$33.8(6) \cdot 10^{0}$	$0.6(2) \cdot 10^{1}$	
$\lvert\sin\Delta\phi_{\mu\mu}\rvert$ <0.75	$84.3(2) \cdot 10^{2}$	$49.8(2) \cdot 10^{2}$	$61.7(4) \cdot 10^{1}$	$19.0(5) \cdot 10^{0}$	$0.3(2) \cdot 10^{1}$	
$\sum p_T^{jets}$ <90 GeV	$44.3(1) \cdot 10^{2}$	$33.0(1) \cdot 10^{2}$	$8.9(2) \cdot 10^{1}$	$10.7(3) \cdot 10^{0}$	$0.3(2) \cdot 10^{1}$	
Δm (130 GeV)	$\mathbf{3.1(1) \cdot 10^{1}}$	$\mathbf{15.1(9) \cdot 10^{0}}$	$\mathbf{7.7(5) \cdot 10^{0}}$	$\mathbf{0.7(3) \cdot 10^{0}}$	$\mathbf{<0.7 \cdot 10^{0}}$	$\mathbf{5.5(2) \cdot 10^{1}}$
Δm (150 GeV)	$\mathbf{14.8(8) \cdot 10^{0}}$	$\mathbf{6.0(6) \cdot 10^{0}}$	$\mathbf{6.2(4) \cdot 10^{0}}$	$\mathbf{0.2(1) \cdot 10^{-1}}$	$\mathbf{<0.7 \cdot 10^{0}}$	$\mathbf{2.8(1) \cdot 10^{1}}$
Δm (200 GeV)	$\mathbf{6.7(5) \cdot 10^{0}}$	$\mathbf{2.0(3) \cdot 10^{0}}$	$\mathbf{5.8(4) \cdot 10^{0}}$	$\mathbf{<0.1 \cdot 10^{-1}}$	$\mathbf{<0.7 \cdot 10^{0}}$	$\mathbf{1.5(1) \cdot 10^{1}}$
Δm (300 GeV)	$\mathbf{2.2(3) \cdot 10^{0}}$	$\mathbf{0.6(2) \cdot 10^{0}}$	$\mathbf{2.3(3) \cdot 10^{0}}$	$\mathbf{<0.1 \cdot 10^{-1}}$	$\mathbf{<0.7 \cdot 10^{0}}$	$\mathbf{5.8(8) \cdot 10^{0}}$
Δm (400 GeV)	$\mathbf{1.1(2) \cdot 10^{0}}$	$\mathbf{0.1(1) \cdot 10^{0}}$	$\mathbf{0.4(1) \cdot 10^{0}}$	$\mathbf{0.1(1) \cdot 10^{-1}}$	$\mathbf{<0.7 \cdot 10^{0}}$	$\mathbf{2.3(7) \cdot 10^{0}}$

Table 4: $\sigma \times BR$ for the background processes obtained after each event selection cut. The upper limits are evaluated at 90% CL. Numbers in brackets represent the statistical error on the last digit.

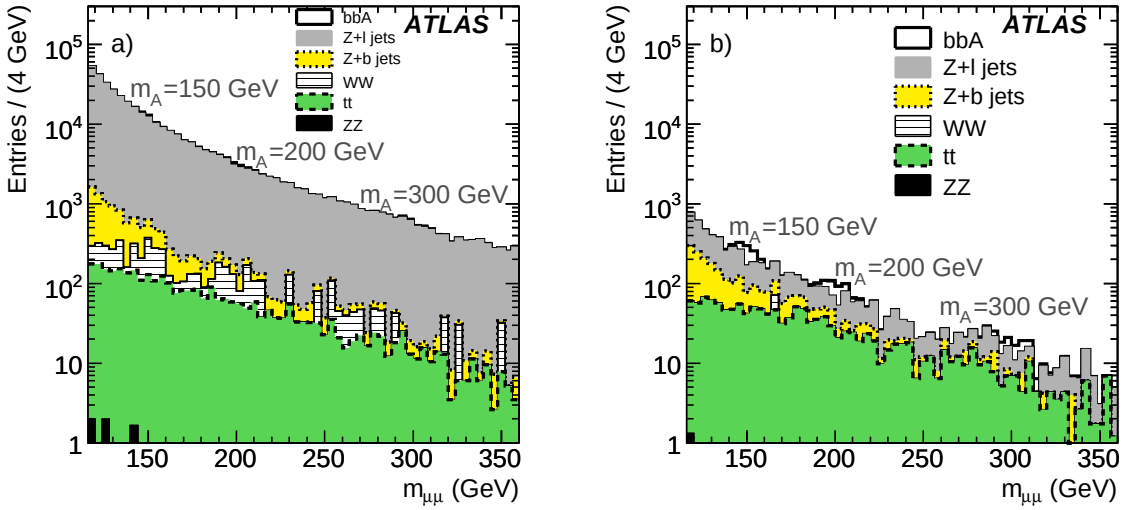

Figure 13: Invariant dimuon mass distributions of the main backgrounds and the A boson signal at masses m_A=150, 200 and 300 GeV and $\tan\beta = 30$, obtained for the integrated luminosity of 30 fb^{-1} . B-tagging has been applied for the event selection. The production rates of H and A bosons have been added together. a) for the 0 b-jet final state and b) for the final state with at least 1 b-jet.

5.3 Trigger selection

Previously calculated event selection efficiencies have been obtained assuming that each analysed event can be triggered. In this Section, a realistic trigger description is included to evaluate the effect of the

limited trigger efficiency on the final event selection.

Since the signal processes are characterized by the two high-p_T muons in the final state (see Figure 9), the most reliable trigger item is a single high-p_T muon with p_T >20 GeV. The single-muon trigger efficiency is mostly limited by the geometrical acceptance of the trigger chambers in the muon spectrometer, as discussed in detail in [29]. The efficiency of the trigger selection for events passing all previously described event selection criteria is shown in Table 5 for the signal at 200 GeV and for the background samples. A very similar trigger selection efficiency can be observed for all signal and

Dataset	L1	High level trigger
$b\bar{b}A$, 200 GeV	97.2	95.0
$t\bar{t}$	97.1	95.1
$b\bar{b}Z$	97.1	94.8

Table 5: Trigger selection efficiency (%) of events which pass all event selection criteria described in Section 5.2. The results are listed for the signal and the two background processes.

background samples. The relatively high final trigger selection efficiency of ∼95% corresponds to the decrease of the signal significance by 2-3% compared to the previously shown results. It has been shown that the observed efficiencies are effectively stable to a level of about ±0.5% at any level of the event selection, since the selection criteria are not affecting the muon kinematics. Furthermore, the trigger selection does not induce any bias to the dimuon invariant mass distribution.

The studies described above have been performed under the assumption that the trigger threshold for a single high-p_T muon is 20 GeV. If this threshold should be higher, some of the signal events might be lost by the trigger selection. In order to evaluate the sensitivity of the signal selection on the varying trigger thresholds, a dedicated study has been performed. New trigger thresholds of 20, 26 and 30 GeV are emulated by the requirement that at least one reconstructed muon with a p_T above the given threshold exists in the event. This muon is also required to have a matching L1 region-of-interest in the muon spectrometer, in order to take into account the holes in the geometrical trigger acceptance. The trigger selection efficiencies for the new trigger thresholds are shown in Figure 14 for events remaining after each of the analysis cuts applied on the $b\bar{b}A$ signal with mass m_A=200 GeV. No visible degradation of the final signal selection is observed for the trigger threshold variations of up to 30 GeV. Similar behavior is observed also for the signal at other mass points. This result can be explained by a rather high muon momenta in the signal samples, such that there is only a small fraction of signal events in which both muons have a p_T below 30 GeV. The dependence of the $t\bar{t}$ and $Zb\bar{b}$ background selection on the trigger threshold of up to 30 GeV is shown to be smaller than 2% after all analysis cuts.

6 Systematic uncertainties

Several sources of systematic uncertainties can affect the total yields of both the signal and the background events after applying the selection criteria specified in the previous Section. In this Section, the influence of the theoretical and the detector-related systematic uncertainties is evaluated.

6.1 Theoretical uncertainties

As mentioned previously, the Higgs boson production in association with the b-quarks has been simulated with PYTHIA and SHERPA Monte Carlo generators and the obtained differential distributions are

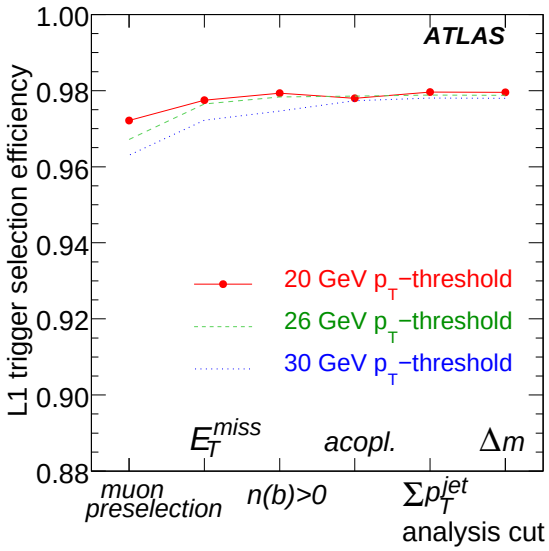

Figure 14: Trigger selection efficiency of the $b\bar{b}A$ signal events (m_A=200 GeV) in dependence on the offline analysis selection. Different curves show the results obtained for different trigger thresholds.

scaled to the Feynhiggs NNLO cross-sections. It is important to remark that no cuts have been applied on the transverse momenta of the generated b-quarks, since also the event topologies with less than two observed b-jets are studied in the presented analyses. (An outgoing b-quark can be considered as observable if its momentum is above ∼15 GeV). Therefore, the corresponding NNLO cross-sections also have to be calculated in an inclusive way, with no constraints on the kinematics of the b-quarks.

As discussed in Section 2, the total theoretical uncertainty on the inclusive cross-section amounts to ∼17%, depending on the Higgs boson mass. In addition, since the experimental search distinguishes between the final states with 0 and those with 1 or more b-jets (with p_T >20 GeV), it is important to show that the proportion between the mentioned different event topologies which is obtained from the Monte Carlo generators also agrees with theory predictions. For this purpose, the fraction of generated events is calculated which have *exactly* one b-quark with p_T >15 GeV and $|\eta|$ <2.5 in the final state (before hadronization). This number is then compared to the ratio of the MCFM cross-section calculated for the $bg \rightarrow bH$ process with the same cuts on the b-quarks, divided by the inclusive cross-section. The result of the comparison is shown in Figure 15, being comparable to the 20% uncertainty. The SHERPA prediction is about 20% higher than PYTHIA and agrees better with the theory calculation with the MRST2004 pdf set. The MRST2002 pdf set gives a better compatibility with PYTHIA. Taking into account the theory uncertainties mentioned above, one can conclude that the samples produced with both generators can reproduce the NLO predictions from a single b-quark rate.

The observed differences between SHERPA and PYTHIA are visible also in the differential b-quark distributions. The differential p_T and η-distributions of the leading b-quark, as obtained by the PYTHIA and SHERPA generators are compared in Figure 16 for the signal at the mass of 200 GeV. The comparison is performed on a parton level, before hadronization. A slightly harder transverse momentum spectrum and a more central pseudorapidity of the b-quarks is observed in the SHERPA events.

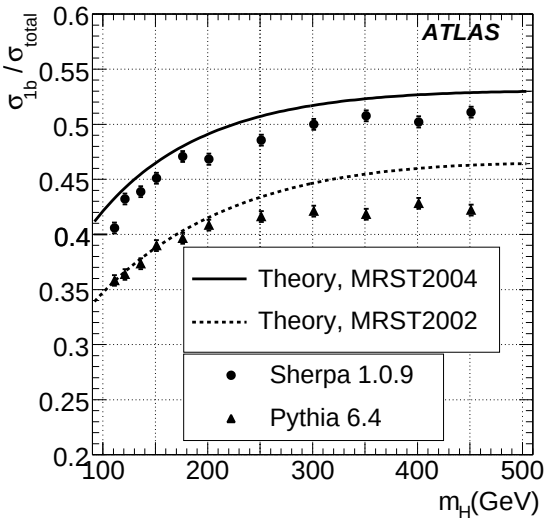

Figure 15: Fraction of events σ_{1b} with exactly one b-quark with p_T >15 GeV and $|\eta|$ <2.5, relative to the total inclusive cross-section σ_{total}, shown in dependence on the Higgs boson mass M_H. The lines show the theory prediction as the ratio between the MCFM $bg \to Hb$ and $b\bar{b} \to H$ cross-sections. Solid line: MRST2004 pdf set, dashed line: MRST2002 pdf set. Circles: result from SHERPA 1.0.9. Triangles: PYTHIA 6.4 $gg \to b\bar{b}H$ process.

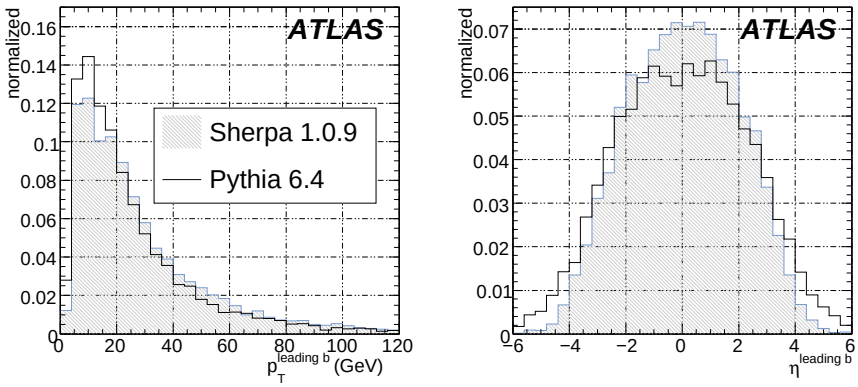

Figure 16: Differential p_T and η distribution of the leading b-quark, obtained by SHERPA (gray histogram) and by the PYTHIA $gg \to b\bar{b}H$ calculation (solid line). All histograms have been normalized to unity.

6.2 Detector-related systematic uncertainties

Systematic uncertainties related to the muon and the jet reconstruction, as well as the uncertainties on the b-tagging performance have been evaluated with rather conservative estimates on the level of understanding of the detector performance. This level is assumed to correspond approximately to an integrated luminosity of 1 fb^{-1}. For each of the above effects, the corresponding change of the reconstructed missing transverse energy is taken into account. Further more, systematic effects due to the differences between the fast and the full simulation are taken into account by means of the comparison between the full and fast simulation.

Muon reconstruction uncertainties are treated separately for the reconstruction efficiency, muon momentum resolution and the muon momentum scale. The efficiency of the muon identification is assumed to be known with an accuracy of $\pm$1%, based on the results of the tag-and-probe method for the muon efficiency measurement from the real data [30]. Systematic errors of the muon momentum scale are taken to be $\pm$1%, arising for instance from the non-perfect knowledge of the magnetic field. The incomplete understanding of the material distributions inside the detector, as well as possible residual detector misalignment can lead to an additional smearing of the muon momentum resolution. Based on early detector calibration, the additional smearing is expected to be $\sigma(\frac{1}{p_T}) = \frac{0.011}{p_T} \oplus 0.00017$ (in 1/(GeV)). The first term enhances the effect of the Coulomb scattering, while the second enhances the contribution from the misalignment.

Jet reconstruction uncertainties are estimated by the jet performance group [25]. In the pseudo-rapidity region below $|\eta|$=3.2, the jet energy scale uncertainty of $\pm$3% and a resolution uncertainty of $\sigma(E) = 0.45 \cdot \sqrt{E}$ are assumed. For $|\eta| >$3.2, the corresponding values are $\pm$10% and $\sigma(E) = 0.63 \cdot \sqrt{E}$ respectively.

b-tagging efficiency and the fake rate are crucial for the described analysis. Conservative relative uncertainty of $\pm$5% on the b-tagging efficiency and $\pm$10% uncertainty on the rejection of the light jets have been assumed.

The results obtained after implementing each of the above systematic uncertainties separately into the analysis are shown in Table 6 for the signal at m_A=150 GeV and for the backgrounds within the corresponding mass window. Signals at different mass points are affected by a similar amount. The

Systematic uncertainty [%]	Signal	$t\bar{t}$	Z+ b jet	Z+light jet
Muon efficiency	$\pm$2	$\pm$1	$\pm$2	$\pm$2
Muon p_T scale	$\pm$2	$\pm$3	$\pm$3	$\pm$5
Muon resolution	-2	-4	3	3
Jet energy scale	$\pm$1	$\pm$5	$\pm$2	$\pm$2
Jet energy resolution	-1	-3	-1	-1
b-tagging efficiency	$\pm$4	$\pm$3	$\pm$4	$\pm$2
b-tagging fake rate	$\pm$1	$\pm$0	$\pm$0	$\pm$6
Full-Atlfast corrections	0	+8	-10	+5
Total	$\pm$5	$\pm$12	$\pm$12	$\pm$11

Table 6: Relative deviation of the selection efficiency in % for the signal at m_A=150 GeV and for the background events after imposing each of the systematic uncertainties separately, as described in the text. The total deviation is given as quadratic sum of the separate contributions, including the one-sided corrections.

background uncertainties are also rather independent of the dimuon mass region, but from one exception. The muon momentum scale mostly affects the background in the lower mass region, close to the Z resonance, while the deviations become smaller for the higher signal masses, i.e. one observes $\pm$11%, $\pm$5% and $\pm$3% for the Higgs masses of 110, 130 and 200 GeV respectively.

7 Background estimation based on the measured data

As previously discussed, theoretical and experimental uncertainties can lead to systematic errors in determination of the background rates. Additional information on the shape and the size of the background contributions can be collected from the real data. As shown before, two major backgrounds surviving all

event selection criteria are the $Z + jet$ and the $t\bar{t}$ processes. Two strategies to estimate their contributions from the measured data shall now be described.

The first method makes use of the fact that the branching ratio for A/H boson decays into two electrons is negligible compared to the dimuon decay channel. Therefore, since one doesn't expect any signal in the dielectron final state, one can use this signature to determine the total background contribution. Additionally, the signatures with one electron and one muon in the final state provide the contribution of the $t\bar{t}$ background alone, since the $Z + jet$ processes do not contribute to this final state. Thus, one can separately measure the two background contributions. The background estimation based on the e^+e^--channel has been discussed in detail in [31]. Good agreement has been demonstrated between the dilepton invariant mass distributions for the $Z \to \mu\mu$ and the $Z \to ee$ processes. In this paper, the emphasis is given to a similar procedure for the determination of the $t\bar{t}$ background.

The goal of the second method is to define a set of event selection criteria which allow for the higher selection efficiency for the particular background process, while simultaneously rejecting all other signal and background contributions. Such background-enriched control sample can be used to better understand the shape of the invariant dimuon mass distribution.

7.1 Background estimation based on the e^+e^- and $\mu^\pm e^\mp$ signatures

The estimation of the $t\bar{t}$ background is important for the analysis channel with at least one b-jet in the final state. A study is performed using fast simulation of the $t\bar{t}$ background, in order to obtain a reliable statistical accuracy. The detector performance given by the fast simulation has been adjusted such to reproduce the performance obtained with the full simulation, as mentioned previously. Based on the studies in [31], the shape of the dilepton invariant mass distribution obtained for the $\mu^+\mu^-$, e^+e^- and $\mu^\pm e^\mp$ final state in the $t\bar{t}$ process are expected to be very similar. The total number of background events selected in each of the three final states will be different due to different reconstruction efficiencies for muons and electrons. However, since these efficiencies can be experimentally measured with an accuracy of better than 1%, this effect can be corrected for rather precisely. Additional differences may occur due to an additional calorimeter activity in presence of electrons. This can be taken into account by rejecting all reconstructed jets which overlap with reconstructed electrons.

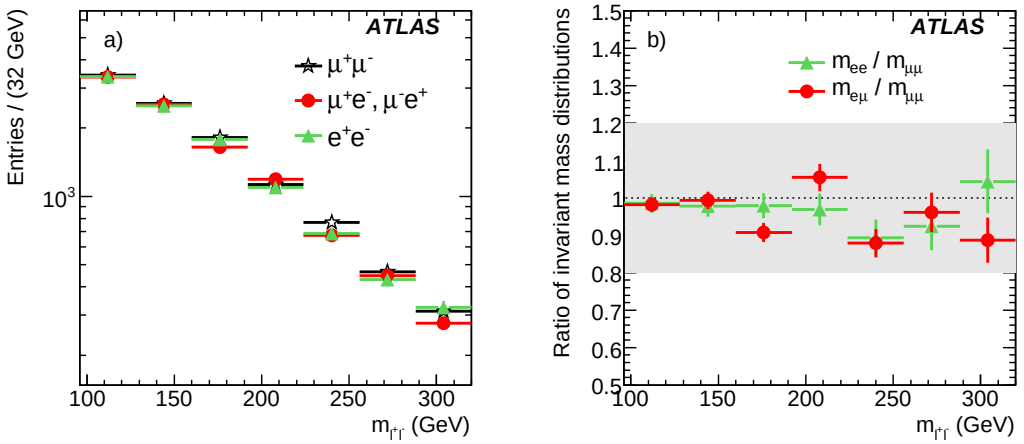

Figure 17: (a) The $\mu^+\mu^-$ invariant mass distribution (stars) of the $t\bar{t}$ background, and its estimates obtained from the e^+e^- (triangles) and $\mu^\pm e^\mp$ (full circles) final states. (b) Corresponding ratios of estimated and actual $\mu^+\mu^-$ invariant mass distributions.

Figure 17(a) shows the invariant mass distributions obtained for the $\mu^+\mu^-$, e^+e^- and $\mu^\pm e^\mp$ final states in $t\bar{t}$ events. The dielectron distribution has been scaled down by a factor 0.84^2, to account for the difference between the electron and muon reconstruction efficiency. Similarly, the $\mu^\pm e^\mp$-distribution has been scaled down by 0.5×0.84. Figure 17(b) shows the corresponding ratios of estimated and actual $\mu^+\mu^-$ invariant mass distribution. The subtraction of the $\mu^\pm e^\mp$ sample from the total background is illustrated in Figure 18 for $\mathscr{L}=30$ fb^{-1}, for the analysis requiring identification of at least one b-jet.

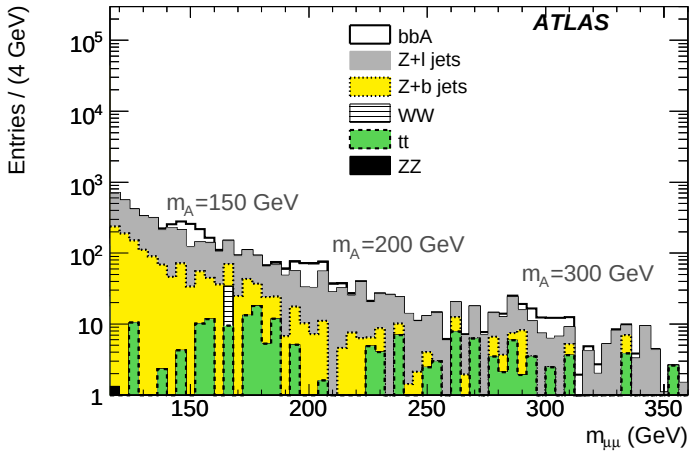

Figure 18: Invariant dimuon mass as in Figure 13(b), after the subtraction of the $t\bar{t}$ background estimated in the $\mu^\pm e^\mp$ final state. The distributions correspond to an integrated luminosity of $\mathscr{L}=30$ fb^{-1}.

7.2 Background estimation from the control samples

In analyses with 0 b-jets in the final state the dominant background is the $Z+jet$ process. Since the topology of this process is very similar to the signal topology, it is rather difficult to define a set of selection criteria which would allow for the extraction of the Z background and simultaneous rejection of the signal.

Contrary to that, the $t\bar{t}$ process is characterized by a relatively high missing transverse energy and a high jet activity. Since this background is important for the analysis with at least one jet in the final state, the event selection criteria of this analysis are modified by selecting only events with a missing transverse energy above 60 GeV and by removing the cut on the $\sum p_T^{jet}$-variable. All other selection criteria remain the same. The purity of the $t\bar{t}$ control sample obtained after the described event selection is shown in Figure 19(a). All remaining processes are suppressed to a negligible amount. Figures 19(b) and (c) show the $t\bar{t}$ background obtained with the selection criteria described in Section 5.2 for at least one b-jet in the final state ($t\bar{t}$ measured) compared to the distribution obtained from the $t\bar{t}$ control sample. Both distributions are normalized to the same number of events. The shape of the $t\bar{t}$ background can be estimated by the described procedure with an accuracy of 10-20%.

7.3 Fit function for the parametrization of the background

The background can be parametrized by the function f_B consisting of a Breit-Wigner and an exponential contribution,

$$f_B(x) = \frac{a_1}{x}\cdot\left[\frac{1}{(x^2-M_Z^2)+M_Z^2\Gamma_Z^2}+a_2\cdot exp(-a_3\cdot x)\right], \quad (1)$$

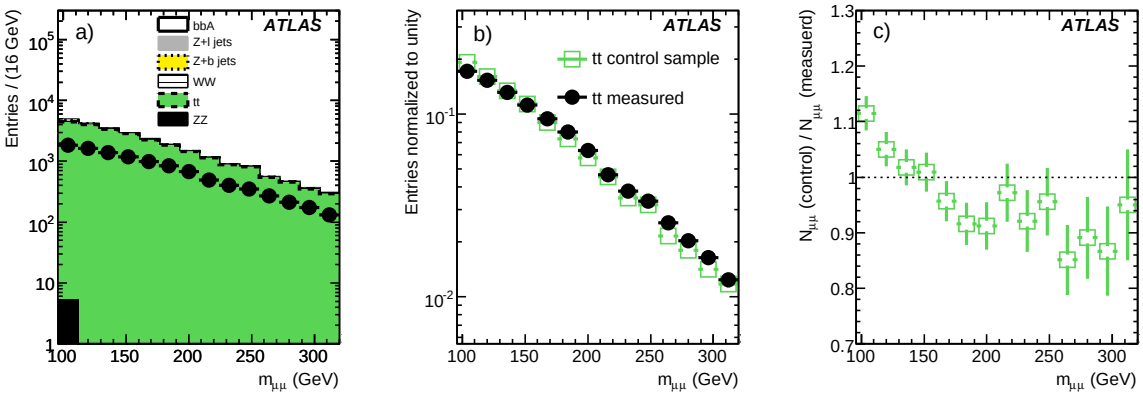

Figure 19: (a) $t\bar{t}$ control sample (stacked histogram) obtained as described in text. Full circles indicate the actually measured $\mu^+\mu^-$ invariant mass distribution for the $t\bar{t}$ background, after applying the standard analysis selection cuts. (b) The measured (full circles) and the control $t\bar{t}$ distributions (open squares), normalized to the same number of events. (c) The ratio of normalized distributions from (b).

where x is the running dimuon mass, while a_1, a_2 and a_3 are the free parametrization parameters. The mean M_Z and the width Γ_Z of the Breit-Wigner distribution describe the Z resonance. The parameters $a_{2,3}$ describing the exponential part can be determined by the fit on the background estimated from data, as described in the previous subsection. The overall normalization factor a_1 is determined by the fit on the side bands of the dimuon mass distribution. Figure 20 shows the result of the fit on the background distribution obtained after all analysis cuts for the case with at least one b-jet in the final state. The two dashed lines correspond to the errors on the $a_{2,3}$ parameters, as obtained from the e^+e^- data at an integrated luminosity of 10 fb^{-1}.

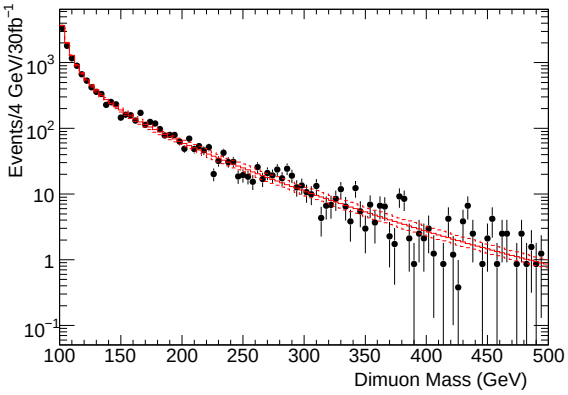

Figure 20: Fit (full line) of the background function f_{bkg} (see Eq. 1) on the background distribution (full circles) resulting from the analysis with at least one b-jet in the final state. The dashed lines represent the shape variations given by the errors on the a_2 and a_3 parameters, from the fit on the e^+e^- data.

The accuracy of the background parametrization by the described method has been tested by means of large number of toy Monte Carlo experiments at different integrated luminosities $\mathscr{L}$. Typical results

of the background extraction in the mass window from 188-212 GeV are shown in Figure 21 for an integrated luminosity of 15 fb^{-1} (left) and 3 fb^{-1} (right). The empirically evaluated expected uncertainty of

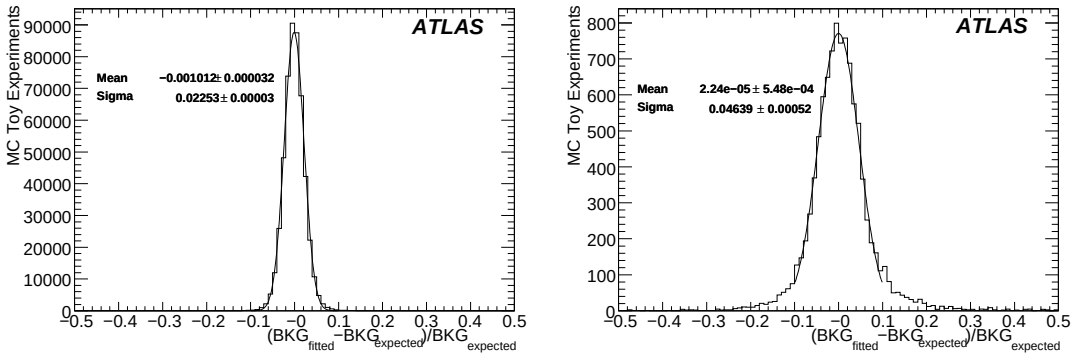

Figure 21: Normalized difference of the expected number of background events ($BKG_{expected}$) in the mass window from 188-212 GeV, and the number (BKG_{fitted}) obtained from the fit method described in the text (left) for an integrated luminosity of =15 fb^{-1} and (b) =3 fb^{-1}.

the background determination from the fit to data is $\sim 8\%/\sqrt{\mathscr{L}[\text{fb}^{-1}]}$. The variation of the exponential shape, due to the errors on the fit parameters a_2 and a_3, plays a non-marginal role only for dimuon masses above 300 GeV, decreasing the relative uncertainty to $\sim 10\%/\sqrt{\mathscr{L}[\text{fb}^{-1}]}$. Conservatively the latter expression will be used in the analyses discussed below. Similar fit procedure has been performed also for the analysis with 0 b-jets in the final state. Due to the larger amount of background, a smaller background uncertainty of $\sim 2\%/\sqrt{\mathscr{L}[\text{fb}^{-1}]}$ can be obtained in this case, including the systematic uncertainty on the shape parameters a_2 and a_3.

8 Evaluation of the signal significance

Two approaches have been applied to evaluate the statistical significance of the observed signal. The "fixed mass" approach provides the significance based on the number of signal and background events which are expected in a given range of the dimuon invariant mass. However, the location of the signal mass peak can be determined only if the signal rates are sufficiently high, or if the signal is already discovered in the $A/H/h \to \tau\tau$ decay channel. In a more general "floating mass" approach, no constraints are applied on the dimuon invariant mass.

The number of signal and background events can be determined from the fit of the function f_{SB} to the data,

$$f_{SB}(x) = p_0 \cdot f_B + p_1 \cdot f_S = p_0 \cdot f_B + p_1 \cdot \frac{1}{\sigma_A\sqrt{2\pi}} \cdot exp\left(-\frac{(x-p_2)^2}{2\sigma_A^2}\right), \quad (2)$$

where f_S is the Gaussian distribution describing the signal. p_2 is the mass of the signal (which can be fixed or left as a free, "floating" parameter) and σ_A is the width of the Higgs resonance. p_0 is the background scale and p_1 the total number of signal events. The number of signal (N_S) and background (N_B) events used for the calculation of the signal significance is extracted from the fit, by integration in a window of $\pm 2\sigma_A$. The signal significance is evaluated by means of the profile likelihood method [32], using the obtained number of signal and background events as an input and taking into account the background uncertainty ($10\%/\sqrt{\mathscr{L}[\text{fb}^{-1}]}$) as discussed in Section 7.3 above.

The results obtained for the signal significance have been cross-checked by the large number of Monte Carlo pseudoexperiments for several different integrated luminosities. The pseudoexperiments

are based on the Monte Carlo distributions and are divided into the "background-only" experiments (*BO*), containing only background contributions, and the "signal-plus-background" experiments (*SpB*) having both the signal and the background contribution. In addition to the profile likelihood calculation in each of these experiments, the signal significance can be estimated also from the log-likelihood ratios. The log-likelihood ratio $\ln Q_{BO}$ and lnQ_{SpB}, both defined as $(N_S+N_B)\ln\frac{N_S+N_B}{N_B}-N_S$, are evaluated for each *BO*- and *SpB*-pseudoexperiment. The signal significance is obtained from the probability of a Type-II error, defined by the fraction of *BO* pseudoexperiments which have a log-likelihood ratio $\ln Q_{BO}$ larger than the median of the $\ln Q_{SpB}$-distribution. The probability of a Type-I error, i.e. the number of *SpB*-pseudoexperiments which fall below the median of the $\ln Q_{BO}$-distribution, was used to determine the 95% CL limits.

Figure 22(left) shows the comparison of the signal significances obtained in the fixed-mass approach. The solid line shows the results of the profile likelihood method, while the dots are the results given by the Type-II error probabilities obtained in the pseudoexperiments. At very low luminosities, the profile-likelihood estimation based on average values seems to slightly overestimate the significance. However, at luminosities close to those needed for the 5σ-significance, the two calculations give equivalent results. Figure 22(right) shows the degradation of the signal significance observed once the floating-mass

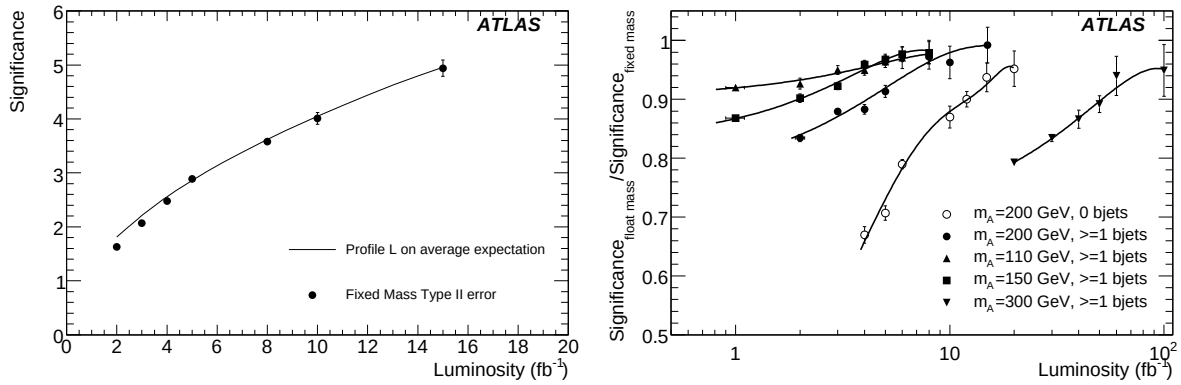

Figure 22: (left) Signal significance obtained in the fixed-mass approach for the signal at m_A=200 GeV and $\tan\beta$=30, as a function of integrated luminosity. The full line corresponds to the results obtained by the profile likelihood method using the average number of expected signal and background events, while the dots show the results obtained from the Type-II error probability from a large amount of pseudoexperiments. Both estimations include the background uncertainty from the f_{SB}-fit. (right) Ratio of signal significances obtained with the floating- and the fixed-mass approach, as a function of the integrated luminosity.

approach is applied in which the Higgs mass is left as a free parameter of the fit (usually reffered to as a look-elsewhere effect). In general, the ratio of the Type-II error probabilities obtained from the fixed-mass and the floating-mass approaches is constant and approximatelly equal to the explored mass range divided by the signal mass width. Correspondingly, the ratio of signal significances is lower at low luminosities, while the difference between the two approaches is reduced to 5% or less at the luminosities close to those needed for a 5σ-discovery.

8.1 Influence of the systematic uncertainties on the signal significance

In order to include the systematic uncertainties in the calculation of the signal significance, one should perform additional large number of pseudoexperiments for each of the systematic effects. However, the

difference between the signal significance in the floating-mass and in the fixed-mass approach is small compared to the effect of the additional systematic uncertainties. Thus, in the following the fixed-mass approach is used and the full treatment of the look-elsewhere effect is left for the future studies.

By means of the background estimation from the data, the amount of the background events underneath the signal can be determined with an accuracy of $\sim 10\%/\sqrt{\mathscr{L}[\text{fb}^{-1}]}$, as described in Section 7. This can be achieved independently of the systematic uncertainties discussed in Section 6.

Therefore, the influence of the systematic uncertainties on the signal significance is given by the corresponding changes in the expected number of signal and background events. The numbers entering the significance calculation are therefore changed accordingly, taking into account that the systematic uncertainty is different for different background processes. The signal significance is calculated separately for each systematic effect and the deviations from the original signal significance are added in quadrature. Figure 23 shows the signal significance obtained for two different masses m_A, as a function of $\tan\beta$. The contributions of the uncertainty in the background determination from the fit to data and of the experimental systematic uncertainties to the expected significance are shown separately.

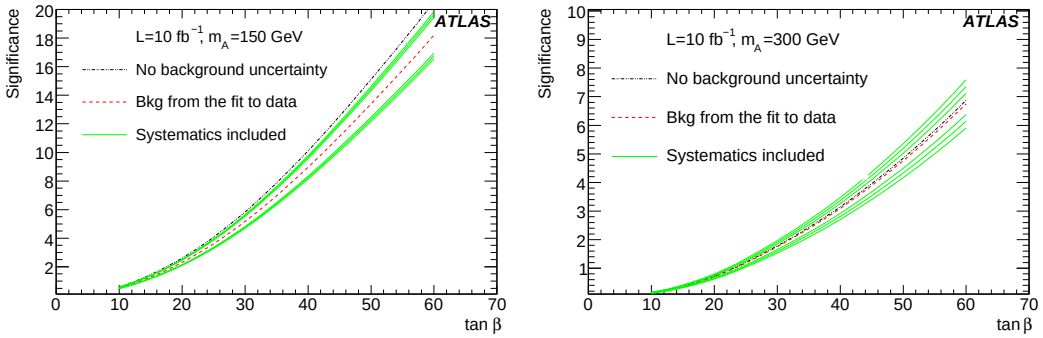

Figure 23: Signal significance as a function of $\tan\beta$ for the integrated luminosity of 10 fb^{-1} and m_A=150 GeV (left) and m_A=300 GeV (right). The dotted curves are obtained assuming a negligible error of the background determination. The dashed curves show the result once the background uncertainty is taken into account, as obtained from the fit to the data. The solid curves additionally include the systematic uncertainties. The width of the solid curves indicates the errors in the background shape parametrization.

9 Discovery potential and the exclusion limits

The previously described methods for the evaluation of the signal significance and of the exclusion limits have been applied to all mass points studied. Table 7 summarizes the signal significances obtained for different signal mass points at $\tan\beta$=30 and $\mathscr{L}$=10 fb^{-1}, for the analysis with 0 b-jets and with at least one b-jet in the final state. The luminosities needed to reach the 5σ signal significance and the 95% CL exclusion limit are given in Table 8, for different signal masses at $\tan\beta$=30. The results shown so far do not include the possible degradation due to the influence of pile-up and cavern background. The degraded resolution of the missing transverse energy is expected to cause a $\sim$15% change in the final selection of the signal and the Z background. The $t\bar{t}$ background is characterized by a large E_T^{miss} and is therefore somewhat less sensitive to the E_T^{miss} performance under pile-up ($\sim$10% change in the selection efficiency). Table 9 summarizes the results obtained with pile-up effects taken into account. Only small changes are observed compared to the previous results.

m_A (GeV)	Signal significance							
	No background uncertainty		Backgr. uncertainty of $10\%/\sqrt{\mathscr{L}[\text{fb}^{-1}]}$		Experimental syst. uncertainty		Theoretical uncertainty	
	0b	$\geq$1b	0b	$\geq$1b	0b	$\geq$1b	0b	$\geq$1b
110	5.5	6.4	2.7	4.5	2.4 - 3.1	3.8 - 5.3	2.2 - 3.2	3.7 - 5.3
130	5.6	6.6	3.6	5.3	3.4 - 3.8	4.8 - 5.9	3.1 - 4.1	4.5 - 6.1
150	5.2	5.8	4.1	5.2	3.9 - 4.3	4.8 - 5.6	3.9 - 4.7	4.5 - 5.9
200	3.1	3.8	2.8	3.6	2.7 - 2.9	3.3 - 3.9	2.5 - 3.1	3.2 - 4.0
300	1.2	1.8	1.1	1.8	1.0 - 1.2	1.6 - 2.0	1.0 - 1.2	1.7 - 1.9
400	0.5	0.8	0.5	0.8	0.4 - 0.5	0.7 - 0.9	0.4 - 0.5	0.7 - 0.9

Table 7: Signal significance for signal at different mass points, with $\tan\beta$=30 and $\mathscr{L}$=10 fb^{-1}. The numbers are shown for different levels of the background uncertainty. For degenerate *A*, *H* and *h* boson states with the same mass, the production rates have been summed.

m_A (GeV)	$\mathscr{L}[\text{fb}^{-1}]$ for a 5σ discovery (No systematics)			$\mathscr{L}[\text{fb}^{-1}]$ for 95% C.L. exclusion					
				No systematics			With systematics		
	0b	$\geq$1b	comb.	0b	$\geq$1b	comb.	0b	$\geq$1b	comb.
110	20.9	12.2	7.7	1.8	2.0	0.9	2.7	2.8	1.4
130	12.0	8.9	5.1	1.9	1.4	0.8	3.6	1.9	1.2
150	10.5	9.3	4.9	1.6	1.5	0.8	2.2	2.0	1.0
200	25.9	19.1	11.0	3.7	3.1	1.7	4.9	3.8	2.1
300	174.6	81.6	55.6	38.6	13.8	10.2	43.8	16.4	12.0
400	1124.0	444.8	318.7	320.0	75.1	60.8	361.0	86.5	69.8

Table 8: Integrated luminosity (in fb^{-1}) needed for a 5σ signal significance and 95% CL exclusion of the signal hypothesis, shown for the signal at $\tan\beta$=30. For degenerate *A*, *H* and *h* boson states with the same mass, the production rates have been summed.

m_A (GeV)	$\mathscr{L}[\text{fb}^{-1}]$ for 5σ discovery	$\mathscr{L}[\text{fb}^{-1}]$ for 95% CL exclusion
110	8.7	1.9
130	5.8	1.6
150	5.6	1.3
200	12.5	2.6
300	62.9	13.6
400	359.5	87.5

Table 9: Luminosity needed for the 5σ signal significance (no systematics) and the 95% CL exclusion of the signal hypothesis (with systematics), obtained for the combined analyses, with the pile-up effects taken into account. The results are shown for $\tan\beta$=30.

The results shown in Tables 7 and 8 can be extrapolated to other $\tan\beta$ values. The only difference which occurs for the a given signal mass point when changing the $\tan\beta$ value is the change of the production rates and of the natural width of the $A/H/h$ bosons. In the $(m_A - \tan\beta)$ plane which is of interest for this analysis, the resolution of the mass measurement is mostly dominated by the experimental resolution. Nevertheless, the variation of the natural Higgs width is taken into account in the calculation

by increasing the background contribution correspondingly to the expected change of the mass window.

Using the previously described production cross-sections and branching ratios, the 5σ-discovery curves are obtained as shown in Figure 24(left) separately for the analysis with 0 and with at least one b-jet in the final state. The luminosity needed for the exclusion of the signal hypothesis at a 95% confidence

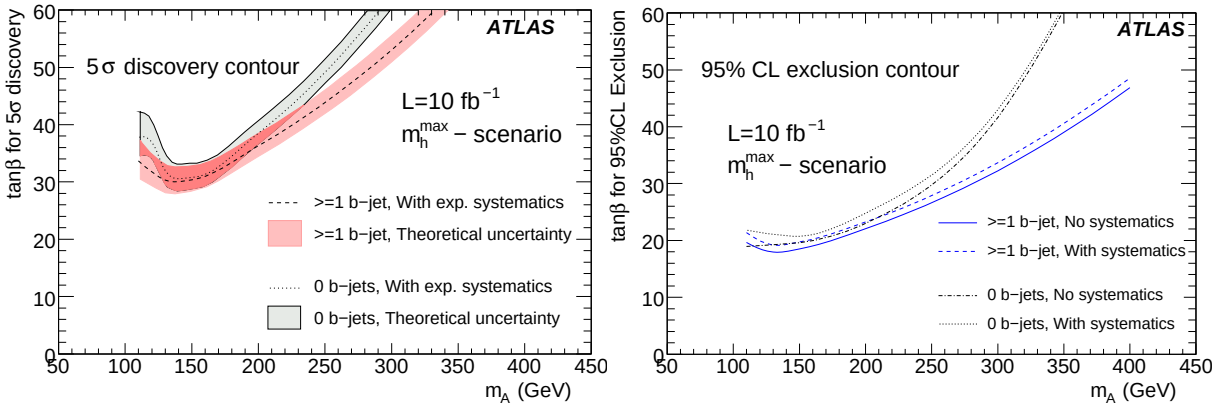

Figure 24: tanβ values needed for the 5σ-discovery (left) and for the 95% CL exclusion of the signal hypothesis (right), shown in dependence on the A boson mass.

level is shown in Figure 24(right).

The signatures with the b-jets in the final state allow for the highest discovery potential. The 0 b-jet final state plays nevertheless an important role. Since the search in this final state is uncorrelated to the previous one, one can quadratically add the signal significances obtained from the two analyses. The 5σ-discovery curves obtained from the combination of both analyses, as well as the combined 95% CL exclusion limits are shown in Figure 25. At an integrated luminosity of 10 fb^{-1}, the discovery can be

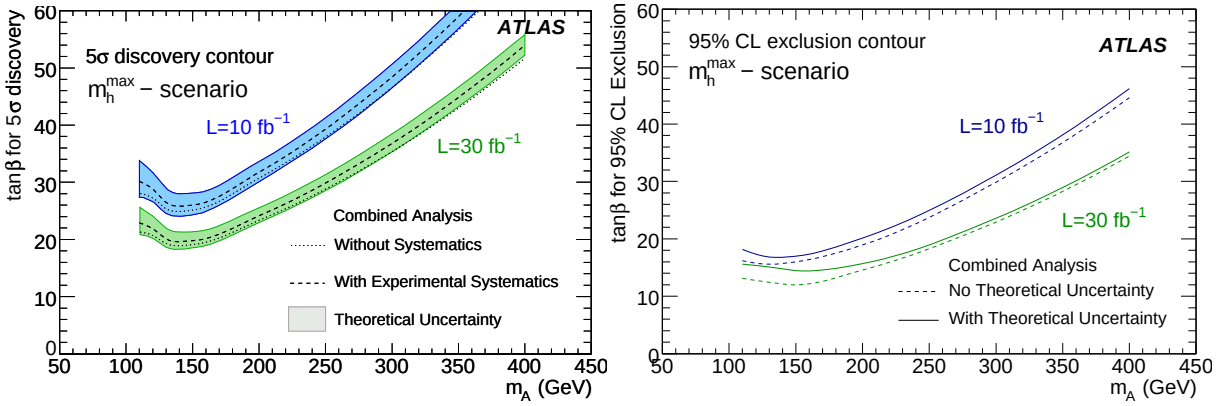

Figure 25: Combined analyses results: (left) tanβ values needed for the 5σ-discovery at $\mathscr{L}$=10 fb^{-1} and $\mathscr{L}$=30 fb^{-1}, shown in dependence on the A boson mass and (right) combined 95% CL exlucion limits.

reached for m_A masses up to 350 GeV with tanβ values between 25 and 60. For m_A masses below 110 GeV the sensitivity drops rapidly as shown in Ref [5], due to the increasing Drell-Yan background close to the pole mass of the Z boson. The tanβ values above $\sim$16 can be excluded already with 10 fb^{-1} of integrated luminosity in case of the Higgs boson masses up to 200 GeV.

10 Conclusions

In this note, the potential for the discovery of the neutral MSSM Higgs boson is evaluated in the dimuon decay channel. As opposed to the Standard Model predictions, the decay of neutral MSSM Higgs bosons A, H and h into two muons is strongly enhanced in the MSSM. In addition, the $\mu^+\mu^-$ final state provides a very clean signature in the detector.

The event selection criteria are optimized in the signal mass range from 100 to 500 GeV, separately for the signatures with 0 b-jets and with at least one b-jet in the final state. The obtained combined result shows that an integrated luminosity of 10 fb^{-1} allows for the discovery for m_A masses up to 350 GeV with $\tan\beta$ values between 30 and 60. Three times higher luminosity allows for an increased sensitivity down to $\tan\beta$=20. The theoretical and detector-related systematic uncertainties are shown to degrade the signal significance by up to 20%. This takes into account that the background contribution can be estimated from the data with an accuracy of $\sim$2-10%/$\mathscr{L}$[fb^{-1}].

References

[1] ATLAS Collaboration, "Introduction on Higgs Boson Searches", this volume.

[2] ATLAS Collaboration, "Discovery Potential of $h/A/H \to \tau^+\tau^- \to \ell^+\ell^- 4\nu$", this volume.

[3] ALEPH, DELPHI, L3 and OPAL Collaborations, The LEP Working Group for Higgs Boson Searches, "Search for neutral MSSM Higgs bosons at LEP", LHWG Note 2005-01.

[4] J. Nielsen, The CDF and D0 Collaborations, "Tevatron searches for Higgs bosons beyond the Standard Model", FERMILAB-CONF-07-415-E, Proceedings of the Hadron Collider Physics Symposium 2007 (HCP 2007), La Biodola, Isola d'Elba, Italy, May 20-26, 2007.

[5] S. Gentile, H. Bilokon, V. Chiarella, G. Nicoletti, *Eur.Phys.J.C* **52** (2007) 229–245.

[6] M. Carena, S. Heinemeyer, C.E.M. Wagner and G. Weiglein, *Eur.Phys.J.C* **26** (2003) 601–607.

[7] S. Heinemeyer, W. Hollik, G. Weiglein, *Comput.Phys.Commun.* **124** (2000) 76–89.

[8] S. Dittmaier, M. Kramer and M. Spira, *Phys.Rev.D* **70** (2004) 074010.

[9] S. Dawson, C.B. Jackson, L. Reina and D. Wackeroth, *Phys.Rev.Lett.* **94** (2005) 031802.

[10] D. Dicus, T. Stelzer, Z. Sullivan and S. Willenbrock, *Phys.Rev.D* **59** (1999) 094016.

[11] R.V. Harlander and W.B. Kilgore, *Phys.Rev.D* **68** (2003) 013001.

[12] K.A. Assamagan et al., "The Higgs Working Group: Summary report 2003", Proceedings of the 3rd Les Houches Workshop: Physics at TeV Colliders, Les Houches, France, 26 May - 6 Jun 2003, *arXiv:0406152 [hep-ph]*.

[13] T. Sjöstrand, P. Eden, C. Friberg, L. Lönnblad, G. Miu, S. Mrenna and E. Norrbin, *Comput.Phys.Commun.* **135** (2001) 238–259.

[14] T. Gleisberg, S. Höche, F. Krauss, A. Schälicke, S. Schumann, J. Winter, *JHEP* **0402** (2004) 056.

[15] S. Catani, F. Krauss, R. Kuhn, and B. R. Webber, *JHEP* **11** (2001) 063.

[16] F. Krauss, A. Schälicke, S. Schumann, G.Soff, *Phys.Rev.D* **70** (2004) 114009.

[17] D. Rebuzzi, M. Schumacher et al., "Cross sections for Standard Model processes to be used in the ATLAS CSC notes", ATL-COM-PHYS-2008-077, Geneva, CERN, 2008.

[18] S. Frixione and B.R. Webber, *JHEP* **0206** (2002) 029;
S. Frixione, P. Nason and B.R. Webber, *JHEP* **0308** (2003) 007.

[19] B.P. Kersevan, E. Richter-Was, *Preprint: TPJU-6-2004, arXiv:0405247 [hep-ph]*.

[20] S. Agostinelli et al., *Nucl.Instrum.Meth.A* **506** (2003) 250-303;
J. Allison et al., *IEEE Transactions on Nuclear Science* **53** No.1 (2006) 270-278.

[21] E. Richter-Was, D. Froidevaux, L. Poggioli, "ATLFAST 2.0 a fast simulation package for ATLAS", ATL-PHYS-98-131, Geneva, CERN, 1998.

[22] ATLAS Collaboration, "Muon Reconstruction and Identification: Studies with Simulated Monte Carlo Samples", this volume;
S. Baranov et al., "Estimation of radiation background, impact on detectors, activation and shielding optimization in ATLAS", ATLAS-GEN-2005-011, Geneva, CERN 2005.

[23] C. Zeitnitz and T.A. Gabriel, *Nucl.Instrum.Meth.A* **349** (1994) 106–111.

[24] A. Fasso, A. Ferrari, J. Ranft, and P.R. Sala, "FLUKA: a multi-particle transport code", CERN-2005-10, Geneva, CERN, 2005.

[25] ATLAS Collaboration, "The ATLAS Experiment at the CERN Large Hadron Collider", JINST 3 (2008) S08003.

[26] ATLAS Collaboration, "Cross-Sections, Monte Carlo Simulations and Systematic Uncertainties", this volume.

[27] ATLAS Collaboration, "*b*-Tagging Performance", this volume.

[28] ATLAS Collaboration, "Measurement of Missing Tranverse Energy", this volume;
ATLAS Collaboration, "Detector Level Jet Corrections", this volume.

[29] ATLAS Collaboration, "Performance of the Muon Trigger Slice with Simulated Data", this volume.

[30] ATLAS Collaboration, "In-Situ Determination of the Performance of the Muon Spectrometer", this volume.

[31] S. Gentile, H. Bilokon, V. Chiarella G. Nicoletti, "Data based method for $Z \rightarrow \mu^+\mu^-$ background subtraction in ATLAS detector at LHC", ATL-PHYS-PUB-2006-019, Geneva, CERN 2006.

[32] W.A. Rolke, A.M. Lopez, J. Conrad, *Nucl.Instrum.Meth.A* **551** (2005) 493–503.